Biogeosciences Discuss., 12, 3943–3990, 2015
www.biogeosciences-discuss.net/12/3943/2015/
doi:10.5194/bgd-12-3943-2015


Biogeosciences Discussions
Open Access



# Changes in dissolved iron deposition to the oceans driven by human activity: a 3-D global modelling study

**S. Myriokefalitakis[1], N. Daskalakis[1,2], N. Mihalopoulos[1,3], A. R. Baker[4], A. Nenes[2,5,6], and M. Kanakidou[1]**

[1]Environmental Chemical Processes Laboratory, Department of Chemistry, University of Crete, P.O. Box 2208, 71003 Heraklion, Greece
[2]Institute of Chemical Engineering Sciences (ICE-HT), FORTH, Patra, Greece
[3]Institute for Environmental Research and Sustainable Development, National Observatory of Athens, Athens, Greece
[4]School of Environmental Sciences, University of East Anglia, Norwich, NR4 7TJ, UK
[5]School of Earth and Atmospheric Sciences, Georgia Institute of Technology, 311 Ferst Drive, Atlanta, GA 30332-0100, USA
[6]School of Chemical and Biomolecular Engineering, Georgia Institute of Technology, 311 Ferst Drive, Atlanta, GA 30332-0100, USA







Received: 31 December 2014 – Accepted: 7 February 2015 – Published: 2 March 2015

Correspondence to: S. Myriokefalitakis (stelios@chemistry.uoc.gr)
and M. Kanakidou (mariak@chemistry.uoc.gr)

Published by Copernicus Publications on behalf of the European Geosciences Union.





BGD
12, 3943–3990, 2015



## Abstract

The global atmospheric iron (Fe) cycle is parameterized in the global 3-D chemical transport model TM4-ECPL to simulate the proton- and the organic ligand-promoted mineral Fe dissolution as well as the aqueous-phase photochemical reactions between the oxidative states of Fe(III/II). Primary emissions of total (TFe) and dissolved (DFe) Fe associated with dust and combustion processes are also taken into account. TFe emissions are calculated to amount to $\sim 35\,\mathrm{Tg\,Fe\,yr^{-1}}$. The model reasonably simulates the available Fe observations, supporting the reliability of the results of this study. Accounting for proton- and organic ligand-promoted Fe-dissolution in present-day TM4-ECPL simulations, the total Fe-dissolution is calculated to be $\sim 0.163\,\mathrm{Tg\,Fe\,yr^{-1}}$ that accounts for up to ~ 50 % of the calculated total DFe emissions. The atmospheric burden of DFe is calculated to be $\sim 0.012\,\mathrm{Tg\,Fe}$. DFe deposition presents strong spatial and temporal variability with an annual deposition flux $\sim 0.489\,\mathrm{Tg\,Fe\,yr^{-1}}$ from which about 25 % ($\sim 0.124\,\mathrm{Tg\,Fe\,yr^{-1}}$) are deposited over the ocean. The impact of air-quality on Fe deposition is studied by performing sensitivity simulations using preindustrial (year 1850), present (year 2008) and future (year 2100) emission scenarios. These simulations indicate that an increase (~ 2 times) in Fe-dissolution may have occurred in the past 150 years due to increasing anthropogenic emissions and thus atmospheric acidity. On the opposite, a decrease (~ 2 times) of Fe-dissolution is projected for near future, since atmospheric acidity is expected to be lower than present-day due to air-quality regulations of anthropogenic emissions. The organic ligand contribution to Fe dissolution shows inverse relationship to the atmospheric acidity thus its importance has decreased since the preindustrial period but is projected to increase in the future. The calculated changes also show that the atmospheric DFe supply to High-Nutrient-Low-Chlorophyll oceanic areas (HNLC) characterized by Fe scarcity, has increased (~ 50 %) since the preindustrial period. However, the DFe deposition flux is expected to decrease (~ 30 %) to almost preindustrial levels over the Northern Hemisphere HNLC oceanic regions in the future. Significant reductions of ~ 20 % over the Southern Ocean





BGD
12, 3943–3990, 2015



and the remote tropical Pacific Ocean are also projected which can further limit the primary productivity over HNLC waters.

## 1 Introduction

Atmospheric deposition of trace constituents, both of natural and anthropogenic origin, can act as a nutrient source into the open ocean and therefore can affect marine ecosystem functioning and subsequently the exchanges of $CO_2$ between the atmosphere and the global ocean (Duce et al., 2008). Aeolian dust deposition, calculated to be $\sim 1257\,\mathrm{Tg\,yr^{-1}}$ (median of 15 global models by Huneeus et al., 2011) and containing $\sim 3.5\,\%$ iron (Fe) on average, is the most significant external supply of Fe in surface waters (Taylor and McLennan, 1985; Mahowald et al., 2005, 2009). As a micronutrient, Fe is limiting phytoplankton productivity in the High-Nutrient-Low-Chlorophyll (HNLC) oceanic regions (i.e. the Southern Ocean, the Eastern equatorial and the Subarctic Pacific; Boyd et al., 2005). The supply of Fe-bearing dust can thus limit primary productivity in large portions of the global ocean, affecting significantly the biological carbon export at the global scale (Maher et al., 2010). At the surface waters, the phytoplankton photosynthetic activity uses $CO_2$ and nutrients to produce biomass and is responsible for nearly half of annual $CO_2$ exchange with the deep-ocean that contains $\sim 85\,\%$ of Earth's mobile carbon (Shao et al., 2011). This is the so-called "biological pump", where the deeper the carbon sinks, the longer it will be removed from the atmosphere (Falkowski et al., 2000). The net result of the biological pump is a continual atmospheric carbon transfer to the deep ocean. The correlation of Fe supply and atmospheric $CO_2$ trapping to the ocean, forms the so-called "Iron Hypothesis" (Martin and Fitzwater, 1988) that initiated significant scientific debate on the potential use of Fe to fertilize the global ocean (i.e. geo-engineering) and consequently increase $CO_2$ storage to the ocean (e.g. Moore and Doney, 2007).

The bioavailable form of Fe that is acquired by phytoplankton is associated with the soluble fraction of Fe, which experimentally is measured as the fraction filterable





BGD
12, 3943–3990, 2015



through 0.2–0.45 µm filters (Kraemer, 2004). Aerosols are emitted or formed, transported and deliquesce in the atmosphere (Raes et al., 2000). Processes that occur in the water associated with aerosols can change aerosol properties. There is experimental evidence that atmospheric acidity is increasing dust solubility (e.g. Nenes et al., 2011) and that present-day atmospheric acidity is mainly driven by air pollution (Seinfeld and Pandis, 1998 and references therein). Although the fraction of soluble Fe in soil is low; atmospheric chemical processes are responsible for Fe conversion to more soluble forms (Mahowald et al., 2005), and thus bioavailable form for the ocean biota. Dust coating by acidic-soluble materials (e.g. nitrates, sulphates) alters also the global pattern of Fe deposition (Fan et al., 2004).

Significant scientific effort has been made to understand the impact of anthropogenically driven atmospheric acidity on dust and parameterise it in the global models. To study the aforementioned changes in dust-Fe solubility driven by human activities, atmospheric models need to account for both (i) the composition of the Fe source and (ii) the atmospheric aging of dust. However, the atmospheric chemical aging of dust with respect to dissolve/bioavailable Fe (hereafter DFe) production is parameterized in chemistry-transport models (CTMs) in different ways. In the modelling study of Meskhidze et al. (2005) Hematite ($Fe_2O_3$) was considered as the only Fe-containing mineral in dust (3 % of Hematite in dust) and the proton-promoted Fe dissolution was described using the empirical parameterisation developed by Lasaga et al. (1994). That study simulated the production of DFe in the ferric oxidation state (Fe(III)) but did not account for any photochemical cycling between Fe(III) and Fe(II). Luo et al. (2008) using the same approximation considered the formation of DFe in the ferrous form (Fe(II)) during Fe-containing minerals dissolution. In support of the proton-promoted Fe dissolution hypothesis, a positive correlation of Fe solubility (SFe; $SFe = 100 \times DFe/TFe$) and sulphur emissions has been observed for acidic atmospheric samples collected at urban sites (Oakes et al., 2012). The simulations by Solmon et al. (2009) suggest that doubling of sulphur emissions can increase the proton-promoted dissolution and deposition of dissolved Fe to the remote Pacific Ocean by ∼ 13 %.





BGD
12, 3943–3990, 2015



Fe dissolution from minerals under acidic conditions occurs in different timescales; from hours to weeks depending on the size and the type of the Fe-containing mineral (Shi et al., 2011a). However, the large acid buffering ability of the carbonate from minerals like $CaCO_3$ and $MgCO_3$ in coarse dust particles can regulate mineral-Fe proton-promoted dissolution, creating an inverse relationship between SFe and particle size (Ito and Feng, 2010). A recent CTM study (Ito and Xu, 2014) predicted the present-day SFe over the Northern Hemisphere oceans reasonably well, and calculated the proton-promoted dissolution of Fe in the year 2100, considering three pools of Fe-containing minerals depending on their timescale of potential for Fe dissolution based on the findings of Shi et al. (2011b, 2012).

Laboratory studies have also shown the occurrence of photoinduced reductive Fe dissolution under rather acidic conditions (e.g. pH < 4), suggesting a steady state Fe(II) production during exposure of dust to solar radiation and thus, increased daytime dissolution rate of Hematite compared to standard kinetics (Zhu et al., 1993; Jickells and Spokes, 2001 and references therein). However, the dust-Fe dissolution through photoreduction has only limited impact (< 1 %) on the DFe concentration (Zhu et al., 1993). Moreover, experimental data also support that both inorganic (e.g. sulphate, ammonium and nitrate) and organic (e.g. oxalate) ligands can increase Fe dissolution (Paris et al., 2011; Paris and Desboeufs, 2013). Oxalic acid/oxalate (hereafter OXL) is globally the most abundant dicarboxylic acid, formed via chemical oxidation of both biogenic and anthropogenic gas-phase precursors in the aqueous-phase of aerosols and cloud droplets (e.g. Carton et al., 2007; Lim et al., 2010). Johnson and Meskindze (2013) calculated that the OXL-promoted Fe dissolution and Fe(II)/Fe(III) redox cycling of Fe-content of mineral dust in both aerosol and cloud water, increased total annual calculated DFe deposition to global oceanic regions by ∼ 75 %, compared to only proton-promoted Fe dissolution simulations. However, that study used sulphate aerosol as a proxy for the occurrence of OXL and took into account three Fe-containing dust-minerals (i.e. goethite, hematite and illite) as studied by Paris et al. (2011).





BGD
12, 3943–3990, 2015



In addition to proton- and ligand-promoted mineral-Fe dissolution, primary emissions of Fe, especially from combustion processes can lead to an increase in the SFe fraction. Mahowald et al. (2009) estimated that although mineral-Fe represents ∼ 95 % of the global atmospheric TFe source, combustion sources of iron are responsible for the remaining ∼ 5 %. In addition, the same study suggested that humans may significantly impact DFe deposition over oceans by increasing both the acidity of atmospheric aerosol, as well as the DFe emissions from combustion. Luo et al. (2008) further accounted for both soluble and insoluble forms of Fe emissions from biomass burning and anthropogenic combustion processes in relation to Black Carbon (BC) emissions and they estimated based on observed Fe/BC ratios that $\sim 1.7\,\mathrm{Tg\,Fe\,yr^{-1}}$ are emitted in the atmosphere via combustion processes, from which ∼ 4 % as DFe from all combustion processes. Model projections for the year 2100 also indicate that fossil fuel combustion aerosols from shipping could contribute up to ∼ 60 % of DFe deposition to remote oceans (Ito, 2013).

In the present study, the 3-D chemical transport global model TM4-ECPL that explicitly calculates aqueous-phase chemistry of OXL and the photochemical cycle of the atmospheric Fe cycle is used to simulate the Fe deposition over land and oceans, accounting for five Fe-containing dust minerals and for anthropogenic emissions of Fe. Following the scheme of Ito and Xu (2014), dissolution of Fe (Sect. 2) from 3 pools of minerals (Shi et al., 2012) is here considered to occur by proton-promoted dissolution at three characteristic time scales and by ligand (OXL)-promoted dissolution (as demonstrated by Paris et al., 2011 and parameterized by Johnson and Meskindze, 2013). The calculated TFe and DFe global atmospheric budgets and distributions are presented and compared to observations in Sect. 3. The importance of air-pollutants on DFe atmospheric concentrations and deposition is investigated in Sect. 4, based on simulations using past and future anthropogenic and biomass burning emissions scenarios. The significant contribution of anthropogenic sources to the solubilization of Fe-containing minerals, their impact on Fe deposition over oceans and the implications of the finding for the biogeochemistry of marine ecosystems are summarized in Sect. 5.





BGD
12, 3943–3990, 2015



## 2 Model description

The TM4-ECPL global chemistry-transport model (Myriokefalitakis et al., 2011; Daskalakis et al., 2014 and references therein) is able to simulate oxidant ($O_3/NO_x/HO_x/CH_4/CO$) chemistry, accounting for non-methane volatile organic compounds (NMVOCs, including isoprene, terpenes and aromatics), as well as all major aerosol components, including secondary aerosols like sulphate ($SO_4^{2-}$), nitrate ($NO_3^-$), ammonium ($NH_4^+$) using ISORROPIA II thermodynamic model (Fountoukis and Nenes, 2007) and secondary organic aerosols (SOA) (Tsigaridis and Kanakidou, 2003, 2007). Compared to its parent TM4 model (van Noije et al., 2004), the current version has a comprehensive description of chemistry (Myriokefalitakis et al., 2008) and organic aerosols (Myriokefalitakis et al., 2010). It also accounts for multiphase chemistry in clouds and aerosol water that produces OXL and affects SOA formation (Myriokefalitakis et al., 2011).

For the present study, TM4-ECPL is driven by ECMWF (European Center for Medium-Range Weather Forecasts) Interim re-analysis project (ERA-Interim) meteorology (Dee et al., 2011). Advection of the tracers in the model is parameterized using the slopes scheme (Russell and Lerner, 1981 and references therein). Convective transport parameterized based on Tiedke (1989) and Olivie et al. (2004) scheme. The vertical diffusion is parameterized as described in Louis (1979). For wet deposition, both large scale and convective precipitation are considered. In-cloud and below cloud scavenging is parameterized in TM4-ECPL as described in detail by Jeuken et al. (2001). In-cloud scavenging of water soluble gases is calculated accounting for the solubility of the gases (effective Henry law coefficients; Tsigaridis et al., 2006; Myriokefalitakis et al., 2011). Dry deposition for all fine aerosol components is parameterized similarly to that of nss-$SO_4^{2-}$, which follows Tsigaridis et al. (2006). Gravitational settling (Seinfeld and Pandis, 1998) is applied to all aerosol components and is the main dry deposition process for coarse particles like dust and sea-salt. The current model configuration has a horizontal resolution of 6° in longitude by 4° in latitude and





BGD
12, 3943–3990, 2015



34 hybrid layers in the vertical, from surface up to 0.1 hPa. All simulations have been performed with meteorology of the year 2008 and a model time-step of 30 min.

### 2.1 Emissions

TM4-ECPL uses the anthropogenic and biomass burning emissions (NMVOC, nitrogen oxides ($NO_x$), CO, $SO_2$, $NH_3$, particulate organic carbon (OC) and black carbon (BC)) from the ACCMIP database (Lamarque et al., 2013). Biogenic emissions (isoprene, terpenes, acetaldehyde, acetone, ethane, ethene, propane, propene, formaldehyde, CO, methyl-ethyl ketone, toluene, methanol) come from the MEGAN – MACC Biogenic Emission Inventory for the year 2008 (Sindelarova et al., 2014). Soil $NO_x$ and oceanic emissions (CO, ethane, ethene, propane, propene) are taken from POET (Granier et al., 2005) inventory database (http://eccad.sedoo.fr). Oceanic emissions of primary organic aerosol, isoprene, terpenes and sea-salt particles are calculated online driven by meteorology following Myriokefalitakis et al. (2010). Dust emissions are obtained from the daily AEROCOM inventories (Aerosol Comparison between Observations and Models; Dentener et al., 2006) updated to the year 2008 (E. Vignatti, personal communication, 2011). The anthropogenic and biomass burning emissions (NMVOC, nitrogen oxides ($NO_x$), CO, $SO_2$, $NH_3$, particulate organic carbon (OC) and black carbon (BC)) from the ACCMIP database (Lamarque et al., 2013) for the years: 1850 (hereafter PAST), 2008 (hereafter PRESENT) and for the year 2100 based on the RCP6 emission scenario (hereafter FUTURE), have been used for the different simulations as further explained. A summary table of the emissions of dust and Fe-containing minerals used in the TM4-ECPL model is provided in Table 1 (all other emissions considered in the model are given in Table S1 in the Supplement).

### 2.2 Dust iron-containing minerals emissions

Various Fe-containing clay minerals (Illite, Kaolinite and Smectite), oxides (Hematite and Goethite) and Feldspars can be found in mineral dust (Nickovic et al., 2013). In the





BGD
12, 3943–3990, 2015



present study, the global soil mineralogy dataset, having the potential to produce dust, developed by Nickovic et al. (2012) at 30 s resolution (~ 1 km) has been re-gridded to $1^{\circ} \times 1^{\circ}$ global resolution and applied to the dust emissions in the TM4-ECPL. Then the percentage content in Fe of the different Fe-containing minerals of dust that are considered in the model has been taken from Nickovic et al. (2013) (Illite 4.8 %, Kaolinite 0.7 %, Smectite 16.4 %, Goethite and Hematite 66 % and Feldspar 2.5 %). Given this, the calculated annual global mean Fe content of dust in TM4-ECPL is ~ 3.1 %. Despite differences in the chemical reactivity of goethite and hematite, these minerals are here considered as one surrogate species, the Hematite, used as proxy for Fe oxides as suggested by Nickovic et al. (2012).

Based on the aforementioned soil mineralogy database ($F_{\mathrm{MIN\_DUST}}$), the daily dust emissions ($\mathrm{Dust_{Emi}}$) in the model and the Fe content of the minerals ($F_{\mathrm{Fe\_MIN}}$), TM4-ECPL calculates the TFe emissions ($\mathrm{Fe_{Emi}}$) from soils as:

$$\mathrm{Fe_{Emi}} = \mathrm{Dust_{Emi}} \cdot F_{\mathrm{MIN\_DUST}} \cdot F_{\mathrm{Fe\_MIN}} \quad (1)$$

Thus, the model accounts for the following annual Fe emissions from soils: $\sim 7.9\,\mathrm{Tg\,Fe\,yr^{-1}}$ Illite, $\sim 0.9\,\mathrm{Tg\,Fe\,yr^{-1}}$ Kaolinite, $\sim 16.1\,\mathrm{Tg\,Fe\,yr^{-1}}$ Smectite, $\sim 5.7\,\mathrm{Tg\,Fe\,yr^{-1}}$ Hematite and Goethite and $\sim 2.8\,\mathrm{Tg\,Fe\,yr^{-1}}$ Feldspar (Table 1), total $\sim 34\,\mathrm{Tg\,Fe\,yr^{-1}}$. The DFe emissions in the form of impurities in soils are prescribed in the initial dust sources as 4.3 % on Kaolinite and 3 % on Feldspar as suggested by Ito and Xu (2014) and account for $\sim 0.12\,\mathrm{Tg\,Fe\,yr^{-1}}$. The annual average surface dust concentrations (Fig. S1a in the Supplement) and Fe concentrations contained in different minerals (Fig. S1b–f) calculated by the model are shown in the Supplement.

### 2.3 Anthropogenic and biomass burning iron emissions

Anthropogenic emissions of TFe from combustion sources have been estimated at $1.07\,\mathrm{Tg\,Fe\,yr^{-1}}$ from biomass burning, $0.66\,\mathrm{Tg\,Fe\,yr^{-1}}$ from coal combustion (Luo et al., 2008) and $\sim 0.016\,\mathrm{Tg\,Fe\,yr^{-1}}$ from shipping (Ito et al., 2013), all for the year 2001. For this, global and monthly mean scaling factors of TFe emissions to those of BC





BGD
12, 3943–3990, 2015



(Fe/BC) for each of the above mentioned emission sectors have been derived based on emission estimates provided by Luo et al. (2008) and the BC sources from the ACCMIP database for the year 2001. Furthermore, to calculate the DFe in primary emissions (both in fine and coarse particles), the DFe emission estimates by Ito (2013) of 0.127 Tg Fe $yr^{-1}$ from biomass burning, 0.055 Tg Fe $yr^{-1}$ from coal combustion and 0.013 Tg Fe $yr^{-1}$ from shipping, have been used together with the TFe emissions above mentioned for the year 2001 (Luo et al., 2008) to derive mean solubility for each of these three emission categories. These are ∼ 12 % for biomass burning Fe sources, ∼ 8 % for coal combustion and ∼ 81 % for shipping. The derived Fe/BC emission ratios and the mean Fe solubility per source category are then applied to the BC emissions from the ACCMIP database for the respective year, to compute the PAST, PRESENT and FUTURE emissions of TFe and DFe. The computed annual mean surface distributions of the TFe emitted by anthropogenic emissions, including shipping, and biomass burning used in the model (∼ 1.8 Tg Fe $yr^{-1}$) for the year 2008 are depicted in Fig. S1g and h, respectively.

### 2.4 Mineral dissolution scheme

The model calculates the dissolution of Fe-containing minerals both in the aerosol water and in the cloud droplets. TM4-ECPL treats the Fe dissolution as a kinetic process that depends on the concentrations of (i) $H^+$ (proton-promoted Fe dissolution) and (ii) OXL (organic ligand-promoted Fe dissolution) in the solution (Fig. 1).

#### 2.4.1 Proton-promoted iron dissolution

The proton-promoted dissolution rate of minerals in aerosol and cloud water is calculated by applying the empirical parameterization developed by Lasaga et al. (1994), taking into account the saturation degree of the solution, the type of each mineral (MIN), as well as the reactivity of Fe species and the ambient temperature.

$$R_{Fe} = NFe_{MIN} \cdot K_{MIN}(T) \cdot a(H^+)^m \cdot f_{MIN} \cdot A_{MIN} \quad (2)$$





BGD
12, 3943–3990, 2015



where $R_{Fe}$ is the Fe-containing mineral dissolution rate (moles Fe (g MIN)$^{-1}$ s$^{-1}$), $NFe_{MIN}$ is the number of moles of Fe per mole of mineral, $K_{MIN}$ is the temperature ($T$) dependent dissolution reaction coefficient of the mineral (mol m$^{-2}$ s$^{-1}$), $\alpha(H^+)$ is the $H^+$ activity in the solution, $m$ is the reaction order with respect to aqueous-phase protons, $A_{MIN}$ is the specific surface area of the mineral (m$^2$ g$^{-1}$), and $f_{MIN}$ accounts for the variation of the rate when deviating from equilibrium. For the present study the above formulation is applied to each mineral concentration [MIN] and not to the bulk mass of dust aerosol, since the model describes each mineral with a different tracer in the chemical scheme. For the calculation of the deviation from equilibrium $f_{MIN}$, the Eq. (3) given by Ito and Xu (2014) is used:

$$f_{MIN} = 1 - \left(a_{Fe^{3+}} \cdot a_{H^+}^{-n_{MIN}}\right) / Keq_{MIN} \quad (3)$$

where $a_{Fe^{3+}}$ is the concentration of Fe(III) in the aqueous solution (mol L$^{-1}$), $n_{MIN}$ is the stoichiometric ratio (number of moles mobilized per mole of mineral) and $Keq_{MIN}$ is the equilibrium constant for iron oxides formation ($Fe(OH)_3$).

Aerosol water pH is calculated by the ISORROPIA II thermodynamic model which solves the $K^+$–$Ca^{2+}$–$Mg^{2+}$–$NH_4^+$–$Na^+$–$SO_4^{2-}$–$NO_3^-$–$Cl^-$–$H_2O$ aerosol system. In order to account for potential neutralization of the acidic species by dust carbonate minerals, dust crustal materials are also taken into account for this study. Based on the composition of mineral dust elements and sea-salt, ISORROPIA II in TM4-ECPL takes into account the following mean percent mass content of particles: $Na^+$: 30.8 % on sea-salt and 1.7 % on dust, $Ca^{2+}$: 4.4 % on dust (as calcite; Meskidze et al., 2005) and 1.2 % on sea-salt, $K^+$: 2.4 % on dust and 1.1 % on sea-salt and $Mg^{2+}$: 1.5 % on dust (as magnesite; Ito and Feng, 2010 – consistent with Formenti et al., 2008 observations) and 3.7 % on sea-salt (http://geology.utah.gov/online_html/pi/pi-39/pi39pg9.htm), $Cl^-$: 55.5 % on sea-salt and $SO_4^{2-}$: 7.7 % on sea-salt. In TM4-ECPL, in-cloud pH is controlled by the strong acids (sulphates, $SO_4^{2-}$; methanesulphonate, $MS^-$; nitric acid, $HNO_3$; nitrate ion, $NO_3^-$) and bases (ammonium ion, $NH_4^+$), and by weak electrolytes. For pH > 4.3 the dis-





BGD
12, 3943–3990, 2015



solution and subsequent dissociation of $CO_2$, $SO_2$, $NH_3$ and OXL are also taken into account (Myriokefalitakis et al., 2011). Note that crustal and sea-salt species are not considered in the cloud chemical scheme. Mineral dissolution rates and the related factors used in this study are listed in Table 2, separating between the DFe (attributed to the emissions), fast released iron ($Fe_f$), intermediate released iron ($Fe_l$) and refractory iron ($Fe_R$) (Shi et al., 2011b, 2012) as explicitly parameterized by Ito and Xu (2014).

### 2.4.2 Organic ligand-promoted iron dissolution

Recent laboratory studies show a positive linear correlation between iron solubility and organic ligands concentrations (e.g. Paris and Desboeufs, 2011 and references therein). Two mechanisms have been proposed concerning the mineral dissolution in the present of organic ligands: (i) the non-reductive (Stumm and Morgan, 1996) and (ii) the reductive (Stumm and Sulzberger, 1992) ligand-promoted dissolution. Paris and Desboeufs (2013) experimental studies support that the released Fe by mineral ligand-promoted dissolution, could be mainly present as dissolved organic Fe(II) complexes because of the ability of organic ligands as electron donors which implies a reductive ligand-promoted dissolution. Moreover, that study also confirms that OXL is the most effective ligand-promoting mineral-Fe solubility among organic binding ligands of Fe, due to its capacity as electron donor.

In the present study we follow the recommendations of Johnson and Meskhidze (2013) based on the experiments by Paris et al. (2011) for OXL-promoted Fe dissolution of Hematite, Goethite and Illite in cloud droplets and rainwater. Because the mineral database used for this study considers the average iron oxides (the goethite and hematite content) as a single iron oxide species, the Hematite, we take into account the fractional OXL-promoted Fe dissolution rates for Hematite ($\alpha$-$Fe_2O_3$) and Goethite ($\alpha$-FeO(OH)) proposed from Johnson and Meskhidze (2013), as presented in Table 3. The average values of relative proportions of Fe in the form of hematite and goethite to total iron oxide are based on experimental data for dust sources, compiled by For-





BGD
12, 3943–3990, 2015



menti et al. (2014), with their abundance in total iron oxide to be ∼ 36 and ∼ 64 %, respectively.

For the present study, the DFe production during the organic ligand-promoted Fe dissolution is considered to be in the form of Fe(II)-oxalato complexes in the aqueous-phase (i.e. in the Ferrus oxidation state) and it is only applied to cloud droplets following the recommendations of the laboratory studies of Paris et al. (2011) and Paris and Desboeufs (2013). Those experiments have been performed with OXL concentrations found typically in rainwater and cloud droplets (0–8 µM), pH of 4.5 and dust concentrations of about 15 mg $L^{-1}$. Indeed, properties of the aqueous solution of clouds differ significantly to those of aerosols, with higher pH values (e.g. > 4), lower aqueous-phase dust concentrations (< 50 mg $L^{-1}$) and lower ionic strength (Shi et al., 2012). On the other hand, the liquid aerosol content of typical continental aerosols can vary between $\sim 10^{-12}$ and $10^{-11}$ $cm^3$ $cm^{-3}$ air, depending on the relative humidity, and the aerosol pH can vary between 1–4 (McNeill et al., 2012). Aqueous-phase OXL concentrations are significantly related to the transfer of small gas-phase polar compounds (e.g. glyoxal) to the liquid-phase (Carlton et al., 2007), a process that depends proportionally on the volume of the aqueous medium and on the pH of the solution. On the other hand, high acidic pH in the condense phase tends to favour the production of oligomeric structures rather than OXL (e.g. Lim et al., 2010, 2013). Thus, under these low pH conditions, the ligand-promoted Fe dissolution may be suppressed significantly.

### 2.5 Aqueous-phase chemistry scheme

The global model simulates aqueous-phase chemistry in aerosol water and cloud droplets as described in Myriokefalitakis et al. (2011). To parameterize the Fe-speciation through the photochemical cycling of Fe(III)/Fe(II), the aqueous-phase chemical scheme has been further developed to account for the mineral-Fe dissolution processes and the Ferric- and Ferrus-oxalato complexes speciation (Fig. 1), taking into account recent global modelling studies (Johnson and Meskhidze, 2013; Lin et al., 2014 and references therein). Here, we use both the proton-promoted dissolution





BGD
12, 3943–3990, 2015



scheme as presented by Ito and Xu (2010) together with the ligand-promoted dissolution scheme as experimentally proposed by Paris et al. (2011). In Table S2 in the Supplement the updates in the chemical scheme of TM4-ECPL concerning Fe chemistry that are adopted for the present study are listed.

## 2.6 Iron dissolution scheme

Johnson and Mekhidze (2013) have concluded that protons effectively promote Fe-containing minerals dissolution at rather acidic pH values ($pH \lesssim 2$), while the OXL-promoted dissolution happens at higher pH values ($pH > 3$). To investigate the sensitivity of our chemical scheme to pH and OXL levels, we have performed box-model simulations to compare the iron solubility from our iron dissolution scheme in different acidic and oxalate-load environments. The box-model calculations have been performed for dust concentrations 1 mg $L^{-1}$ and pH values of 1.5, 4.5 and 8.5 for oxalic acid concentrations of 0, 4.5 and 8 µM. The percentage content in Fe in dust has been taken from Nickovic et al. (2013) as in the global TM4-ECPL model. Moreover, to take into account the Fe speciation due to aqueous-phase photochemical reactions, the box model also considers $[H_2O_2] = 1$ µM, $[O_3] = 10^{-6}$ µM, $[OH] = 10^{-7}$ µM and $[HO_2] = 10^{-7}$ µM. In Fig. S9, the SFe calculated by each of our box-model simulations is presented.

According to our calculations after 10 days of processing, in the absence of OXL concentrations but in highly acidic pH values of 1.5, the SFe is calculated to reach ~ 10 % (Fig. S9a), while at pH = 4.5 the SFe is reaching only ~ 1 % and at highly basic pH values of 8.5 the SFe barely reaches 0.03 %. In the presence of OXL concentration of 4.5 µM, the box-model calculates no significant change of SFe for highly acidic pH of 1.5 compared to the absence of OXL at the same pH, while for pH = 4.5 the SFe reaches ~ 4 % and for pH = 8.5 the SFe is raised up to 7 %. This can be explained because in highly basic pH values the mole fractions of oxalate are higher compared to less basic and strong acidic pH values and thus, the ligand-promoted dissolution tends to be less effective, as already noted by Johnson and Meskhidze (2013). In the case of high oxalic acid concentrations of 8 µM (Fig. S9), the box-model calculates that





BGD
12, 3943–3990, 2015



Fe dissolution is the more effectively promoted by ligands than by protons. Indeed, for pH = 8.5 and [OXL] = 8 µM (Fig. S9b), the box model calculates that SFe reaches ∼ 10 %, as in the case of highly acidic pH in the absence of OXL (Fig. S9a). However, for pH = 1.5 and [OXL] = 8 µM the SFe reaches also high values that can be only attributed to the proton-promoted dissolution since the mole fraction of oxalate is extremely low in these pH values. In contrast, for the case of a mid-range pH value (4.5), SFe reaches ∼ 7 % as result of mainly ligand promoted dissolution and to a lesser extend to the proton promoted one (Fig. S9b and a).

Although the aforementioned sensitivity box-modeling studies show the significance between the proton- and ligand-promoted Fe dissolution depending on the chemical conditions, the proton-promoted dissolution is expected to be more important in the atmospheric conditions. While high basic pH values are associated only with dust alkalinity (Ito and Feng, 2010) located close to dust sources, no significant oxalic acid sources, which are controlled mainly from biogenic NMVOC emissions (Myriokefalitakis et al., 2011) and cloudiness, are expected to be found near the desert regions (e.g. the Sahara).

## 3 Results and discussion

### 3.1 Primary and secondary sources of dissolved iron

In Fig. 2, the annual mean primary DFe emissions from anthropogenic (Fig. 2a), biomass burning (Fig. 2b) and from Fe-contacting minerals (Fig. 2c) sources are shown together with the annual mean total mineral Fe-dissolution flux (sum of proton- and organic ligand-promoted Fe dissolution fluxes; secondary DFe sources) as calculated by the model (Fig. 2d). The model takes into account $\sim 0.071\,\mathrm{Tg\,Fe\,yr^{-1}}$ of DFe anthropogenic emissions with most of them to occur over densely populated regions of the globe (e.g. China, Europe and the US), but also in the remote oceans (e.g. Northern Atlantic Ocean, Northern Pacific Ocean), due to oil-combustion processes downwind





BGD
12, 3943–3990, 2015



the shipping lanes. Primary emissions of DFe from biomass burning (Fig. 2b) peak over tropical forested areas in contrast to those from anthropogenic activities that peak over the mid-latitudes of the Northern Hemisphere. According to model calculations, biomass burning contributes about $\sim 0.127\,\mathrm{Tg\,Fe\,yr^{-1}}$, showing maxima over Central Africa and Amazonia during the dry season. DFe emissions associated with mineral dust (Fig. 2c) of $\sim 0.128\,\mathrm{Tg\,Fe\,yr^{-1}}$, are emitted mainly over the Saharan desert region but, important emissions are also found over other desert areas of the globe (e.g. the Gobi Desert, Middle East and Australia).

The secondary sources of DFe in the atmosphere result from both the proton- and ligand-promoted dissolution processes of Fe-containing mineral in the model (Fig. 2d). The total annual mineral Fe-dissolution flux is calculated to be $\sim 0.163\,\mathrm{Tg\,Fe\,yr^{-1}}$ of DFe by TM4-ECPL. As shown in Fig. 2d, most of the dissolution occurs downwind of the dust source region, where long- and regional-range transport of natural and anthropogenic pollution sources enhance the release of DFe from the minerals. Thus, the model calculates maximum dissolution fluxes downwind the Sahara like the Mediterranean Basin, the Gobi desert, over the tropical Atlantic Ocean, the Middle East and India and the outflow of Asia to the Pacific Ocean.

### 3.2 Proton- vs. organic ligand-promoted mineral iron mobilisation

The proton- and the ligand-promoted dissolution of Fe-containing minerals are compared in Fig. 3a and b, respectively. According to TM4-ECPL calculations on global scale, $\sim 80\,\%$ of dust Fe dissolution occurs through proton-promoted dissolution of Fe (Fig. 3a; $\sim 0.129\,\mathrm{Tg\,Fe\,yr^{-1}}$), where high proton concentrations destabilize Fe-oxygen (Fe-O) bonds in the crystal lattice of the mineral Fe containing minerals. Proton-promoted Fe dissolution dominates downwind to dust source areas and heavy population regions (close to $1.00\,\mathrm{ng\,Fe\,m^{-2}\,s^{-1}}$) where atmospheric acidity is high due to $SO_x$ and $NO_x$ anthropogenic emissions. On the other hand, relatively high rates of organic ligand-promoted dissolution (Fig. 3b) are calculated over Amazonia (close to





BGD
12, 3943–3990, 2015



0.05 ng Fe $m^{-2}$ $s^{-1}$), where high biogenic NMVOC oxidation and cloudiness lead to enhanced OXL aqueous-phase formation (Myriokefalitakis et al., 2011).

### 3.3 Iron concentrations

The calculated global annual mean TFe and DFe atmospheric surface distributions are shown in Fig. 4a and b, respectively, (the dissolved Fe(III) and Fe(II) in Fig. S2a–b and S2c–d in the Supplement, respectively), and the fractions of Fe(II) to DFe are presented in Fig. 4c (note differences in scales). Maxima annual mean concentrations of more than 100 µg Fe $m^{-3}$ air are calculated to occur over the Sahara and Gobi deserts near the surface. The outflow from these source regions transports TFe over the global ocean, with the highest impact calculated for the Northern Hemisphere (Fig. 4a). African Fe sources also affect the middle troposphere through atmospheric transport along the tropical Hadley cell (Fig. S2b and d).

The DFe concentrations (sum of Fe(III) and Fe(II)) are calculated to be about three orders of magnitude lower than the TFe (Fig. S2a and c). As for TFe, the outflow from the continental source regions is clearly seen in the calculated DFe distributions. Model calculations also demonstrate the importance of photochemical redox cycling of Fe(III)/Fe(II) in the aqueous-phase (aerosols and clouds) of the atmosphere. Figure S2c and d denote that calculated Fe(II) concentrations are an important part of DFe atmospheric burden, regionally reaching up to 50 % of the total dissolved mass far from the dust source areas e.g. the remote ocean. The enhanced concentrations of Fe(III) over polluted regions, such as Mexico ($\sim$ 40 ng Fe $m^{-3}$) determine the importance of atmospheric acidity and anthropogenic DFe emissions (Fig. S2a). Over Central South America, Asia and Indonesia, high concentrations of DFe ($\sim$ 50–100 ng Fe $m^{-3}$) are calculated both due to biomass burning DFe emissions but also due to organic ligand-promoted dissolution, which is enhanced in these areas by the OXL produced from oxidation of emitted biogenic NMVOCs via clouds. Fe(III) (Fig. S2b) and Fe(II) (Fig. S2d) show significant concentrations in the middle troposphere owing to transport from the





BGD
12, 3943–3990, 2015



source regions but also from in-cloud and in aerosol water chemical processing that transforms part of TFe to DFe in the atmosphere. Figure 4c shows the percentage contribution of Fe(II) to DFe as computed by the model for the surface and the zonal mean distribution. This ratio exceeds ~ 10 % at several locations around the globe in particular over remote oceanic regions, as for instance in the tropical Pacific and the tropical North Atlantic Ocean. This implies that chemical aging of dust due to long-range transport enhances significantly the Fe(II) production.

TM4-ECPL calculates a global TFe atmospheric burden of ~ 0.454 Tg Fe and almost 40 times lower atmospheric burden of the DFe ~ 0.012 Tg Fe (~ 0.011 Tg Fe as Fe(III) and ~ 0.001 Tg Fe as Fe(II)). This denotes an overall fractional solubility for atmospheric Fe of ~ 2.6 % and also indicates the existence of a large TFe reservoir that can be mobilized under favourable conditions. The average lifetime of TFe ($\tau_{TFe}$) is calculated to be about 5 days while that of DFe ($\tau_{DFe}$) is found to be longer (~ 6 days on average) due to its association with atmospheric aerosol that has been transported and processed in the atmosphere and thus resides overall in smaller size aerosols than TFe. DFe residing mostly in small particles is more effectively transported in the atmosphere reaching the global ocean than the bulk TFe mass that is carried mainly by coarse aerosols.

### 3.4 Model iron concentration evaluation

Observations of total and dissolved Fe concentrations in ambient aerosols near the surface are valuable to evaluate our understanding of the Fe cycle as parameterized in the models. TM4-ECPL results are here validated against observations of total (Fig. 5a) and dissolved Fe (Fig. 5b) associated with atmospheric aerosols over the Atlantic Ocean (Baker et al., 2013) and the Indian Ocean (Witt et al., 2006) as compiled by Sholkovitz et al. (2013). In addition, Fe aerosol data compiled by Mahowland et al. (2005) are compared with model results in Fig. 5c. All evaluations (see Table S3 in the Supplement) are based on statistical parameters of correlation coefficient ($R$;





BGD
12, 3943–3990, 2015



Eq. S1), normalised mean bias (NMB; Eq. S2), root mean square error (RMSE; Eq. S3), and normalised mean error (NME; Eq. S3).

The seasonality of TFe in the East Mediterranean as measured and compiled by Koulouri et al. (2008) at Finokalia station (http://finokalia.chemistry.uoc.gr/) is also compared to model results as shown in Fig. 5d. The comparisons presented in Fig. 5 show that the model reasonably simulates the observed concentration of total and dissolved Fe in the ambient aerosols over oceans (scatter plots in Fig. 5a–c). In the East Mediterranean, when comparing to ambient aerosol observations at Finokalia monitoring station (Fig. 4d), the model seems to underestimate the observations of TFe with the largest differences calculated for January–February, May and July–September. These are the periods of the year that Finokalia station can be occasionally affected by strong dust outbreaks from Africa that are better represented in the observations than in the model results due to their episodic character.

### 3.5 Iron deposition

TM4-ECPL calculates that $\sim 34\,\mathrm{Tg\,Fe\,yr^{-1}}$ of TFe are deposited to the Earth's surface (Fig. 6a). The highest annual deposition fluxes of TFe of $\sim 100\,\mathrm{ng\,Fe\,m^{-2}\,s^{-1}}$ (i.e. $\sim 3.2\,\mathrm{g\,Fe\,m^{-2}\,yr^{-1}}$) are calculated to occur over the Sahara and Gobi deserts near the surface. Significant deposition fluxes up to $\sim 10\,\mathrm{ng\,Fe\,m^{-2}\,s^{-1}}$ are calculated at the outflow from these source regions, with the highest outflow impact calculated for the Northern Hemisphere over the outflows of Atlantic and Pacific Oceans. The global DFe deposition is calculated to be $\sim 0.489\,\mathrm{Tg\,Fe\,yr^{-1}}$ of which $\sim 0.124\,\mathrm{Tg\,Fe\,yr^{-1}}$ is deposited over the global ocean (Fig. 6b). This oceanic DFe deposition estimate is lower to an earlier reported global oceanic DFe deposition flux of $0.26\,\mathrm{Tg\,Fe\,yr^{-1}}$ according to Johnson and Meskhidze (2013). However, that study used dust emissions of $\sim 1900\,\mathrm{Tg\,yr^{-1}}$ that is about 60 % larger that the dust sources the TM4-ECPL takes into account for this work ($\sim 1090\,\mathrm{Tg\,yr^{-1}}$ for the year 2008).

Figures 6c–f present the seasonal variability of DFe deposition as calculated by TM4-ECPL. The maximum seasonal DFe deposition flux of $\sim 0.136\,\mathrm{Tg\,Fe}$ is calculated to oc-





BGD
12, 3943–3990, 2015



cur during JJA (June-July-August; Fig. 6e), followed by the flux of ∼ 0.127 Tg Fe during MAM (March-April-May; Fig. 6d). During the aforementioned periods, the enhanced photochemistry over the Northern Hemisphere increases the atmospherically-driven acidity due to $NO_x$ and $SO_x$ oxidation, and thus enhances proton-dissolution of mineral dust. Moreover, OXL aqueous-phase formation and therefore organic ligand-promoted Fe dissolution is favoured due to the enhanced biogenic NMVOC emissions during the warm season (Myriokefalitakis et al., 2011). On the contrary, during SON (September-October-November; Fig. 6f) and DJF (December-January-February; Fig. 6c), the model calculates lower DFe deposition fluxes, of ∼ 0.104 Tg Fe season$^{-1}$ and ∼ 0.122 Tg Fe season$^{-1}$, respectively, due to the slower photochemical activity and therefore the lower Fe dissolution fluxes of both from proton- and organic ligand-promoted dissolution. Note, also, that most dust and TFe emissions are occurring in the mid-latitudes of the Northern Hemisphere where the majority of anthropogenic emissions of acidity precursors are occurring (Fig. S1).

### 3.6 Model iron deposition evaluation

In Fig. 7, TM4-ECPL deposition fluxes of TFe and DFe (this work) are compared to the estimates over four Atlantic Ocean regions (Fig. S10) based on the observations of Baker et al. (2013) as well as the deposition fields from the modelling studies of Mahowald et al. (2009) and Johnson et al. (2010) as compiled and presented by Baker et al. (2013). Both of these modelling studies assumed a constant Fe content of 3.5 % in dust and a proton-promoted Fe dissolution. DFe deposition fluxes have been calculated for 4 regions as described in Baker et al. (2013), with Region 2 corresponding to North Atlantic dry regions, Region 3 corresponding to intertropical convergence zone (ITCZ), Region 4 to South Atlantic dry regions and Region 5 to South Atlantic storm rainfall (Fig. S10). In the South Atlantic (Region 4) during the dry season (AMJ; April-May-June) TM4-ECPL calculations of TFe deposition show a broad agreement with the measurements and also agree with the other modelling studies. On the other hand, the model overestimates the measurements of TFe in Region 2 and Region 3





BGD
12, 3943–3990, 2015



during the AMJ, similarly to the modelling study by Mahowald et al. (2009). During the wet season (SON; September-October-November; Fig. 7b), TM4-ECPL overestimates the measured values from Baker et al. (2013), similarly to the modelling study by Mahowald et al. (2009). For Region 4 during SON the model agrees well with the Baker et al. (2013) and calculates lower TFe deposition fluxes compared to Mahowald et al. (2009) but very close to the estimation from Johnson et al. (2010). TM4-ECPL model overestimates the observed DFe deposition over Regions 2, 3 and 4 during both studied periods, while it underestimates DFe deposition over Region 5, similarly to other model estimates (Fig. 7c and d).

## 4 Sensitivity of dissolved iron to air-pollutants

The response of mineral-Fe dissolution to the changes in emissions is here assessed by comparing simulations performed using anthropogenic and biomass burning PAST and FUTURE emissions (see Sect. 2). Atmospheric acidity strongly depends on $SO_x$ and $NO_x$ anthropogenic emissions and Fe solubility is impacted by atmospheric acidity as discussed above. Minerals dissolution is therefore expected to be significantly affected by anthropogenic emissions. Iron anthropogenic and biomass burning emissions also vary as shown in Table 1 and explained in Sect. 2.3. Note, however, that meteorology, dust emissions and biogenic NMVOC emissions (and thus OXL formation from biogenic sources) are constant for both PAST and FUTURE simulations, corresponding to the year 2008 (i.e. PRESENT simulation). Thus the computed changes presented in Fig. 8 are due only to emission changes.

### 4.1 Past and future changes in iron dissolution

For the PAST simulation, the anthropogenic emissions (e.g. $NO_x$, $NH_x$ and $SO_x$) are a factor of 5–10 lower than present day emissions (Lamarque et al., 2010). Thus, compared to the present day, the model calculates significant changes in the aerosol-phase





BGD
12, 3943–3990, 2015



pH in the PAST simulation with less acidic (aerosol and cloud) pH over the surface Northern Hemisphere oceans but a more acidic pH, over Europe due to extensive coal combustion in 1850 (Fig. S4a in the Supplement). FUTURE simulation projects in general a less acidic aerosol pH (Fig. S4b) when compared to the present-day simulation, owing to lower $NO_x$ and $SO_x$ emissions. Indeed, for the FUTURE simulation, anthropogenic emissions for most of the continental areas are projected to be lower than the present-day and to almost return to pre-1980 levels due to air quality regulations (Lamarque et al., 2013).

Past and future changes of the atmospheric acidity have a significant effect on mineral-Fe dissolution. For the PAST simulation the model calculates about three-times lower proton-promoted mineral Fe dissolution ($\sim 0.041\,\mathrm{Tg\,Fe\,yr^{-1}}$) compared to the PRESENT ($\sim 0.129\,\mathrm{yr^{-1}}$) (Fig. 8a). As far as the FUTURE simulation is concerned, proton-promoted mineral Fe dissolution ($\sim 0.039\,\mathrm{Tg\,Fe\,yr^{-1}}$) is also projected to be about three times lower than at present (Fig. 8b).

In parallel to the aforementioned computed differences due to atmospheric acidity, changes in the contribution of organic-ligand to the total mineral-Fe dissolution are also computed. The organic ligand-promoted mineral-Fe dissolution process is calculated to gain importance for the total dissolution flux (Fig. 8c and d), showing an inverse pattern compared to the proton-promoted one. Differences in the pH of atmospheric (aerosol and cloud) water and oxidant levels can affect significantly OXL aqueous-phase chemical production (Myriokefalitakis et al., 2011). According to TM4-ECPL calculations the increase in OXL levels can enhance significantly the organic-ligand promoted Fe-mineral dissolution in remote oceanic regions with very low dust load. However, dust load over the remote oceans could increase if dust outbreaks become more important in the future (Goudie, 2009).

One other aspect of the organic ligand-promoted mineral-Fe dissolution is also the effect on the speciation of dissolved and bioavalable Fe. According to chemical scheme of this work, the production of Fe(II)-oxalato complexes increases significantly the Ferrus content in the DFe, in contrast to the proton-promoted mineral-Fe dissolution





BGD
12, 3943–3990, 2015



where Fe(III)-complexes dominate total DFe production. Indeed, when only the proton-promoted Fe dissolution is considered in our model, the Ferrus-complexes are produced during the day, when the Fe(III) is converted into Fe(II) as a result of the Fe(III) photolysis as also the Deguillaume et al. (2004) proposed. However, when the organic ligand Fe-dissolution is taken into account, the Fe(II) is increased, since there is production of Ferrus-complexes even without sunlight. This can explain also the observed high Fe(II) content compared to Fe(III) in the DFe in precipitation over the Mediterranean (Theodosi et al., 2010). The relative contribution of these two types of dissolution can be also seen by the percentage differences of PAST and FUTURE ferric and ferrous fractions, respectively, in the calculated DFe (Fig. S7). TM4-ECPL calculates that the decrease in the atmospheric acidity both in the PAST and in the FUTURE simulations increases the importance of organic-ligand mineral-Fe dissolution and thus leads to a significant enhancement of the Fe(II) content in DFe (Fig. S7a and b) and a simultaneous reduction of Fe(III) (Fig. S7c and d).

### 4.2 Past and future changes in iron deposition

The model calculates DFe deposition flux of $\sim 0.230\,\mathrm{Tg\,Fe\,yr^{-1}}$ (with $\sim 0.050\,\mathrm{Tg\,Fe\,yr^{-1}}$ over oceans) in the PAST that is lower (Fig. S8a, negative differences) compared to PRESENT ($\sim 0.489\,\mathrm{Tg\,Fe\,yr^{-1}}$ with $\sim 0.124\,\mathrm{Tg\,Fe\,yr^{-1}}$ over oceans). Differences are also apparent for the SFe (Fig. S8c), with by up to $\sim 80\,\%$ lower values in the PAST compared to PRESENT over the global oceans as well as over highly populated regions of the world. This can be explained by the weaker acidification of mineral dust in the PAST than in the PRESENT atmosphere (also shown by the negative changes from present day in $SO_4^{2-}$ and $NO_3^-$ surface concentrations in Fig. S3a and c in the Supplement). Note, however, that significantly lower amounts of combustion aerosols Fe are simulated to be emitted in the PAST simulation (see Table 1). FUTURE DFe deposition is calculated to be $\sim 0.372\,\mathrm{Tg\,Fe\,yr^{-1}}$ (with $\sim 0.088\,\mathrm{Tg\,Fe\,yr^{-1}}$ over oceans) which is lower than the simulated global PRESENT deposition (Fig. 8f). The reduction in SFe compared to present day (Fig. S8d) is calculated to be up to $\sim 70\,\%$ over the





BGD
12, 3943–3990, 2015



mid-latitudes of the Northern Hemisphere and up to 50 % over the Southern Hemisphere and the tropical-subtropical oceanic regions.

### 4.3 Biogeochemical implications

The determination of iron solubility is important to understand the carbon biogeochemical cycle. However, in order to estimate the impact of Fe on the ocean productivity, and thus on the impact on Earth's climate system, the study of DFe deposition has to be focused of the HNLC waters such as the Southern Ocean (Boyd et al., 2000), since the current major dust deposition oceanic regions (e.g. the Atlantic Ocean downwind to Sahara) are already dust-Fe saturated and no significant biogeochemical implications are expected due to changes in Fe dissolution there. Thus, for the present study the differences on Fe deposition are also calculated for the HNLC water where Fe is expected to limit the primary productivity. For the characterization of HNLC oceanic regions, the annual mean global $NO_3^-$ surface water concentrations from the LEVITUS94 World Ocean Atlas (http://iridl.ldeo.columbia.edu/SOURCES/.LEVITUS94/) and the monthly chlorophyll *a* (Chl *a*) concentrations MODIS retrievals taken into account in the model (Myriokefalitakis et al., 2010) for the year 2008 are used. The model grid boxes corresponding to HNLC waters are here defined based on the co-occurrence of surface seawater $NO_3^-$ concentrations of $> 4$ mM (Duce et al., 2008) and Chl *a* concentrations of $< 0.1\,\mathrm{mg\,m^{-3}}$ (Boyd et al., 2007).

The deposition fluxes of TFe and DFe over HNLC waters are presented in Fig. 9a and b, respectively. The model calculates that $\sim 0.478\,\mathrm{Tg\,Fe\,yr^{-1}}$ of TFe are deposited over the HNLC ocean with the maximum deposition fluxes to be calculated over the Northern Pacific Ocean ($\sim$ 5–10 $\mathrm{ng\,Fe\,m^{-2}\,s^{-1}}$) and the lowest over the Southern Ocean ($\sim$ 0.05–0.5 $\mathrm{ng\,Fe\,m^{-2}\,s^{-1}}$). The same pattern is also calculated for the DFe deposition with higher deposition fluxes over the Northern Pacific Ocean ($\sim 0.05\,\mathrm{ng\,Fe\,m^{-2}\,s^{-1}}$) and lower over the Southern Ocean ($\sim 0.005\,\mathrm{ng\,Fe\,m^{-2}\,s^{-1}}$). TM4-ECPL calculates a depo-





BGD
12, 3943–3990, 2015



sition flux of ~ 0.021 Tg Fe yr$^{-1}$ of DFe over the HNLC waters which represents ~ 17 % of the total oceanic DFe deposition flux but only ~ 4 % of the global one.

The percentage differences of calculated PRESENT DFe deposition fluxes from the PAST and FUTURE simulations over the HNLC oceans are depicted in Fig. 9c and d, respectively. The model in general calculates for both PAST and FUTURE simulation lower DFe deposition fluxes over the HNLC waters. An increase of ~ 50 % is calculated to have happened the latest 150 years (PAST vs. PRESENT simulation, Fig. 9c) which can be attributed to the increase of mineral Fe dissolution and (to a lesser extent) the increase of primary DFe emission from both anthropogenic and biomass burning sources. Furthermore, significant decreases in DFe deposition over the HNLC oceans are calculated for the FUTURE simulation, although with smaller changes than those computed for the PAST simulation. The decrease in mineral Fe dissolution due to air-quality legislations projected for the future atmosphere leads to a reduction of DFe deposition of ~ 30 % over the Northern HNLC oceanic regions (i.e. North Pacific and North Atlantic) and ~ 20 % over the remote tropical Pacific Ocean and the Southern Ocean. The sensitivity PRESENT-to-FUTURE simulations clearly support that changes in atmospheric acidity and Fe combustion sources driven by anthropogenic emissions affect the DFe deposition over HNLC waters and have the potential to perturb open-ocean phytoplankton blooms and thus the carbon biogeochemical cycling.

## 5 Conclusions

Primary dust emissions (minerals) and anthropogenic and biomass-burning (combustion) sources of TFe and DFe as well as atmospheric processing by proton- and organic ligand-promoted mineral Fe-dissolution and aqueous-phase photochemical reactions between different forms of Fe(III/II) are accounted for in the state-of-the-art chemistry transport model TM4-ECPL. The model calculates for present day conditions an atmospheric Fe dissolution flux of ~ 0.163 Tg Fe yr$^{-1}$ of which ~ 20 % is attributed to the impact of organic ligands on the Fe cycle. The atmospheric burden of DFe is calculated





BGD
12, 3943–3990, 2015



to be ~ 0.012 Tg Fe and the dissolved Fe annual deposition flux over the oceans to be ~ 0.124 Tg Fe $yr^{-1}$. Sensitivity simulations show that increases in anthropogenic emissions since 1850 resulted in more acidic environment and thus an increase (~ 50 %) in DFe deposition (~ 0.230 Tg Fe $yr^{-1}$ in the past against ~ 0.489 Tg Fe $yr^{-1}$ nowadays). Air quality regulations are projected to also decrease anthropogenic emissions and thus atmospheric acidity in 2100. Our model results indicate that this will lead to reduced mineral Fe dissolution (~ 0.076 Tg Fe $yr^{-1}$) compared to the present one (~ 0.163 Tg Fe $yr^{-1}$), as well as a lower DFe deposition (~ 0.372 Tg Fe $yr^{-1}$). Focusing on the HNLC waters, an increase in DFe deposition of ~ 50 % is calculated for the last 150 years but a decrease of ~ 20 % over the Southern Ocean is projected for the future. In view of the importance of Fe as micronutrient for the marine ecosystems, the calculated past, present and future changes in Fe solubility indicate the necessity of the implementation of comprehensive dust dissolution processes in carbon-climate coupled models by taking into account the air-quality changes in the global atmosphere.

**The Supplement related to this article is available online at doi:10.5194/bgd-12-3943-2015-supplement.**

*Acknowledgements.* This research has been co-financed by the European Union (European Social Fund – ESF) and Greek national funds through the Operational Program "Education and Lifelong Learning" of the National Strategic Reference Framework (NSRF) – Research Funding Program: ARISTEIA – PANOPLY (Pollution Alters Natural Aerosol Composition: implications for Ocean Productivity, cLimate and air qualitY) grant.

## References

Baker, A. R., Adams, C., Bell, T. G., Jickells, T. D., and Ganzeveld, L.: Estimation of atmospheric nutrient inputs to the Atlantic Ocean from 50° N to 50° S based on large-scale field





BGD
12, 3943–3990, 2015



sampling: iron and other dust-associated elements, Global Biogeochem. Cy., 27, 755–767, doi:10.1002/gbc.20062, 2013.
Bonneville, S., Vancappellen, P., and Behrends, T.: Microbial reduction of iron(III) oxyhydroxides: effects of mineral solubility and availability, Chem. Geol., 212, 255–268, doi:10.1016/j.chemgeo.2004.08.015, 2004.
Boyd, P. W., Watson, A. J., Law, C. S., Abraham, E. R., Trull, T., Murdoch, R., Bakker, D. C., Bowie, A. R., Buesseler, K. O., Chang, H., Charette, M., Croot, P., Downing, K., Frew, R., Gall, M., Hadfield, M., Hall, J., Harvey, M., Jameson, G., LaRoche, J., Liddicoat, M., Ling, R., Maldonado, M. T., McKay, R. M., Nodder, S., Pickmere, S., Pridmore, R., Rintoul, S., Safi, K., Sutton, P., Strzepek, R., Tanneberger, K., Turner, S., Waite, A., and Zeldis, J.: A mesoscale phytoplankton bloom in the polar Southern Ocean stimulated by iron fertilization, Nature, 407, 695–702, doi:10.1038/35037500, 2000.
Boyd, P. W., Strzepek, R., Takeda, S., Wong, C. S., and McKay, R. M.: The evolution and termination of an iron-induced mesoscale bloom in the northeast subarctic Pacific, Limnol. Oceanogr., 50, 1872–1886, 2005.
Boyd, P. W., Jickells, T., Law, C. S., Blain, S., Boyle, E. A., Buesseler, K. O., Coale, K. H., Cullen, J. J., de Baar, H. J. W., Follows, M., Harvey, M., Lancelot, C., Levasseur, M., Owens, N. P. J., Pollard, R., Rivkin, R. B., Sarmiento, J., Schoemann, V., Smetacek, V., Takeda, S., Tsuda, A., Turner, S., Watson, A. J.: Mesoscale iron enrichment experiments 1993–2005: synthesis and future directions, Science, 315, 612, doi:10.1126/science.1131669, 2007.
Carlton, A. G., Turpin, B. J., Altieri, K. E., Seitzinger, S., Reff, A., Lim, H.-J., and Ervens, B.: Atmospheric oxalic acid and SOA production from glyoxal: results of aqueous photooxidation experiments, Atmos. Environ., 41, 7588–7602, 2007.
Daskalakis, N., Myriokefalitakis, S., and Kanakidou, M.: Sensitivity of tropospheric loads and lifetimes of short lived pollutants to fire emissions, Atmos. Chem. Phys. Discuss., 14, 22639–22676, doi:10.5194/acpd-14-22639-2014, 2014.
Dee, D. P., Uppala, S. M., Simmons, A. J., Berrisford, P., Poli, P., Kobayashi, S., Andrae, U., Balmaseda, M. A., Balsamo, G., Bauer, P., Bechtold, P., Beljaars, A. C. M., van de Berg, L., Bidlot, J., Bormann, N., Delsol, C., Dragani, R., Fuentes, M., Geer, A. J., Haimberger, L., Healy, S. B., Hersbach, H., Hólm, E. V., Isaksen, L., Kållberg, P., Köhler, M., Matricardi, M., McNally, A. P., Monge-Sanz, B. M., Morcrette, J. J., Park, B. K., Peubey, C., de Rosnay, P., Tavolato, C., Thépaut, J. N., and Vitart, F.: The ERA-Interim reanalysis: configuration





BGD
12, 3943–3990, 2015



and performance of the data assimilation system, Q. J. Roy. Meteor. Soc., 137, 553–597, doi:10.1002/qj.828, 2011.
Deguillaume, L., Leriche, M., Monod, A., and Chaumerliac, N.: The role of transition metal ions on $HO_x$ radicals in clouds: a numerical evaluation of its impact on multiphase chemistry, Atmos. Chem. Phys., 4, 95–110, doi:10.5194/acp-4-95-2004, 2004.
Dentener, F., Kinne, S., Bond, T., Boucher, O., Cofala, J., Generoso, S., Ginoux, P., Gong, S., Hoelzemann, J. J., Ito, A., Marelli, L., Penner, J. E., Putaud, J.-P., Textor, C., Schulz, M., van der Werf, G. R., and Wilson, J.: Emissions of primary aerosol and precursor gases in the years 2000 and 1750 prescribed data-sets for AeroCom, Atmos. Chem. Phys., 6, 4321–4344, doi:10.5194/acp-6-4321-2006, 2006.
Duce, R. A., LaRoche, J., Altieri, K., Arrigo, K. R., Baker, A. R., Capone, D. G., Cornell, S., Dentener, F., Galloway, J., Ganeshram, R. S., Geider, R. J., Jickells, T., Kuypers, M. M., Langlois, R., Liss, P. S., Liu, S. M., Middelburg, J. J., Moore, C. M., Nickovic, S., Oschlies, A., Pedersen, T., Prospero, J., Schlitzer, R., Seitzinger, S., Sorensen, L. L., Uematsu, M., Ulloa, O., Voss, M., Ward, B., and Zamora, L.: Impacts of atmospheric anthropogenic nitrogen on the open ocean, Science, 320, 893, doi:10.1126/science.1150369, 2008.
Falkowski, P., Scholes, R. J., Boyle, E., Canadell, J., Canfield, D., Elser, J., Gruber, N., Hibbard, K., Högberg, P., Linder, S., Mackenzie, F. T., Moore III, B., Pedersen, T., Rosenthal, Y., Seitzinger, S., Smetacek, V., and Steffen, W.: The global carbon cycle: a test of our knowledge of Earth as a system, Science, 290, 291–296, doi:10.1126/science.290.5490.291, 2000.
Fan, S.-M.: Impact of air pollution on wet deposition of mineral dust aerosols, Geophys. Res. Lett., 31, L02104, doi:10.1029/2003GL018501, 2004.
Formenti, P., Rajot, J. L., Desboeufs, K., Caquineau, S., Chevaillier, S., Nava, S., Gaudichet, A., Journet, E., Triquet, S., Alfaro, S., Chiari, M., Haywood, J., Coe, H., and Highwood, E.: Regional variability of the composition of mineral dust from western Africa: results from the AMMA SOP0/DABEX and DODO field campaigns, J. Geophys. Res., 113, D00C13, doi:10.1029/2008JD009903, 2008.
Formenti, P., Caquineau, S., Desboeufs, K., Klaver, A., Chevaillier, S., Journet, E., and Rajot, J. L.: Mapping the physico-chemical properties of mineral dust in western Africa: mineralogical composition, Atmos. Chem. Phys., 14, 10663–10686, doi:10.5194/acp-14-10663-2014, 2014.





BGD
12, 3943–3990, 2015



Fountoukis, C. and Nenes, A.: ISORROPIA II: a computationally efficient thermodynamic equilibrium model for $K^+$–$Ca^{2+}$–$Mg^{2+}$–$NH_4^+$–$Na^+$–$SO_4^{2-}$–$NO_3^-$–$Cl^-$–$H_2O$ aerosols, Atmos. Chem. Phys., 7, 4639–4659, doi:10.5194/acp-7-4639-2007, 2007.

Granier, C., Guenther, A., Lamarque, J., Mieville, A., Muller, J., Olivier, J., Orlando, J., Peters, J., Petron, G., Tyndall, G., and Wallens, S.: POET, a database of surface emissions of ozone precursors, available at: http://www.aero.jussieu.fr/projet/ACCENT/POET.php (last access: December 2014), 2005.

Goudie, S.: Dust storms: recent developments, J. Environ. Manage., 90, 89–94, doi:10.1016/j.jenvman.2008.07.007, 2009.

Huneeus, N., Schulz, M., Balkanski, Y., Griesfeller, J., Prospero, J., Kinne, S., Bauer, S., Boucher, O., Chin, M., Dentener, F., Diehl, T., Easter, R., Fillmore, D., Ghan, S., Ginoux, P., Grini, A., Horowitz, L., Koch, D., Krol, M. C., Landing, W., Liu, X., Mahowald, N., Miller, R., Morcrette, J.-J., Myhre, G., Penner, J., Perlwitz, J., Stier, P., Takemura, T., and Zender, C. S.: Global dust model intercomparison in AeroCom phase I, Atmos. Chem. Phys., 11, 7781–7816, doi:10.5194/acp-11-7781-2011, 2011.

Ito, A.: Global modeling study of potentially bioavailable iron input from shipboard aerosol sources to the ocean, Global Biogeochem. Cy., 27, 1–10, doi:10.1029/2012GB004378, 2013.

Ito, A. and Feng, Y.: Role of dust alkalinity in acid mobilization of iron, Atmos. Chem. Phys., 10, 9237–9250, doi:10.5194/acp-10-9237-2010, 2010.

Ito, A. and Xu, L.: Response of acid mobilization of iron-containing mineral dust to improvement of air quality projected in the future, Atmos. Chem. Phys., 14, 3441–3459, doi:10.5194/acp-14-3441-2014, 2014.

Jeuken, A., Veefkind, J. P., Dentener, F., Metzger, S., and Roble Gonzalez, C.: Simulation of the aerosol optical depth ocer Europe for August 1997 and a comparison with observations, J. Geophys. Res., 106, 28295–28311, 2001.

Jickells, T. D. and Spokes, L. J.: Atmospheric iron inputs to the oceans, in: The Biogeochemistry of Iron in Seawater, edited by: Turner, D. R. and Hunter, K., SCOR/IUPAC Series, John Wiley & Sons, New York, 85–121, 2001.

Johnson, M. S. and Meskhidze, N.: Atmospheric dissolved iron deposition to the global oceans: effects of oxalate-promoted Fe dissolution, photochemical redox cycling, and dust mineralogy, Geosci. Model Dev., 6, 1137–1155, doi:10.5194/gmd-6-1137-2013, 2013.





BGD
12, 3943–3990, 2015



Johnson, M. S., Meskhidze, N., Solmon, F., Gasso, S., Chuang, P. Y., Gaiero, D. M., Yantosca, R. M., Wu, S., Wang, Y., and Carouge, C.: Modeling dust and soluble iron deposition to the South Atlantic Ocean, J. Geophys. Res., 115, D15202, doi:10.1029/2009JD013311, 2010.

Kraemer, S. M.: Iron oxide dissolution and solubility in the presence of siderophores, Aquat. Sci.-Res. Across Boundaries, 66, 3–18, doi:10.1007/s00027-003-0690-5, 2004.

Koulouri, E., Saarikoski, S., Theodosi, C., Markaki, Z., Gerasopoulos, E., Kouvarakis, G., Mäkelä, T., Hillamo, R. and Mihalopoulos, N.: Chemical composition and sources of fine and coarse aerosol particles in the Eastern Mediterranean, Atmos. Environ., 42, 6542–6550, doi:10.1016/j.atmosenv.2008.04.010, 2008.

Lamarque, J.-F., Bond, T. C., Eyring, V., Granier, C., Heil, A., Klimont, Z., Lee, D., Liousse, C., Mieville, A., Owen, B., Schultz, M. G., Shindell, D., Smith, S. J., Stehfest, E., Van Aardenne, J., Cooper, O. R., Kainuma, M., Mahowald, N., McConnell, J. R., Naik, V., Riahi, K., and van Vuuren, D. P.: Historical (1850–2000) gridded anthropogenic and biomass burning emissions of reactive gases and aerosols: methodology and application, Atmos. Chem. Phys., 10, 7017–7039, doi:10.5194/acp-10-7017-2010, 2010.

Lamarque, J.-F., Dentener, F., McConnell, J., Ro, C.-U., Shaw, M., Vet, R., Bergmann, D., Cameron-Smith, P., Dalsoren, S., Doherty, R., Faluvegi, G., Ghan, S. J., Josse, B., Lee, Y. H., MacKenzie, I. A., Plummer, D., Shindell, D. T., Skeie, R. B., Stevenson, D. S., Strode, S., Zeng, G., Curran, M., Dahl-Jensen, D., Das, S., Fritzsche, D., and Nolan, M.: Multi-model mean nitrogen and sulfur deposition from the Atmospheric Chemistry and Climate Model Intercomparison Project (ACCMIP): evaluation of historical and projected future changes, Atmos. Chem. Phys., 13, 7997–8018, doi:10.5194/acp-13-7997-2013, 2013.

Lanzl, C. A., Baltrusaitis, J. and Cwiertny, D. M.: Dissolution of hematite nanoparticle aggregates: influence of primary particle size, dissolution mechanism, and solution pH, Langmuir, 28, 15797–808, doi:10.1021/la3022497, 2012.

Lasaga, A. C., Soler, J. M., Ganor, J., Burch, T. E., and Nagy, K. L.: Chemical-weathering rate laws and global geochemical cycles, Geochim. Cosmochim. Ac., 58, 2361–2386, 1994.

Lim, Y. B., Tan, Y., Perri, M. J., Seitzinger, S. P., and Turpin, B. J.: Aqueous chemistry and its role in secondary organic aerosol (SOA) formation, Atmos. Chem. Phys., 10, 10521–10539, doi:10.5194/acp-10-10521-2010, 2010.





BGD
12, 3943–3990, 2015



Lim, Y. B., Tan, Y., and Turpin, B. J.: Chemical insights, explicit chemistry, and yields of secondary organic aerosol from OH radical oxidation of methylglyoxal and glyoxal in the aqueous phase, Atmos. Chem. Phys., 13, 8651–8667, doi:10.5194/acp-13-8651-2013, 2013.

Lin, G., Sillman, S., Penner, J. E., and Ito, A.: Global modeling of SOA: the use of different mechanisms for aqueous-phase formation, Atmos. Chem. Phys., 14, 5451–5475, doi:10.5194/acp-14-5451-2014, 2014.

Louis, J.-F.: A parametric model of vertical eddy fluxes in the atmosphere, Bound.-Lay. Meteorol., 17, 187–202, 1979.

Luo, C., Mahowald, N. M., Meskhidze, N., Chen, Y., Siefert, R. L., Baker, A. R., and Johansen, A. M.: Estimation of iron solubility from observations and a global aerosol model, J. Geophys. Res., 110, D23307, doi:10.1029/2005JD006059, 2005.

Luo, C., Mahowald, N., Bond, T., Chuang, P. Y., Artaxo, P., Siefert, R., Chen, Y., and Schauer, J.: Combustion iron distribution and deposition, Global Biogeochem. Cy., 22, GB1012, doi:10.1029/2007GB002964, 2008.

Maher, B. A., Prospero, J. M. Mackie, D., Gaiero, D., Hesse, P. P., and Balkanski, Y.: Global connections between aeolian dust, climate and ocean biogeochemistry at the present day and at the last glacial maximum, Earth-Sci. Rev., 99, 61–97, doi:10.1016/j.earscirev.2009.12.001, 2010.

Mahowald, N. M., Baker, A. R., Bergametti, G., Brooks, N., Duce, R. A., Jickells, T. D., Kubilay, N., Prospero, J. M., and Tegen, I.: The atmospheric global dust cycle and iron inputs to the ocean, Global Biogeochem. Cy., 19, GB4025, doi:10.1029/2004GB002402, 2005.

Mahowald, N., Engelstaedter, S., Luo, C., Sealy, A., Artaxo, P., Benitez-Nelson, C., Bonnet, S., Chen, Y., Chuang, P. Y., Cohen, D. D., Dulac, F., Herut, B., Johansen, A. M., Kubilay, N., Losno, R., Maenhaut, W., Paytan, A., Prospero, J. M., Shank, L. M., and Siefert, R. L.: Atmospheric iron deposition: global distribution, variability and human perturbations, Annu. Rev. Mar. Sci., 1, 245–278, doi:10.1146/annurev.marine.010908.163727, 2009.

Martin, J. H. and Fitzwater, S. E.: Iron deficiency limits phytoplankton growth in the north-east Pacific subarctic, Nature, 331, 341–343, doi:10.1038/331341a0, 1988.

McNeill, V. F., Woo, J. L., Kim, D. D., Schwier, A. N., Wannell, N. J., Sumner, A. J., and Barakat, J. M.: Aqueous-phase secondary organic aerosol and organosulfate formation in atmospheric aerosols: a modeling study, Environ. Sci. Technol., 46, 8075–8081, doi:10.1021/es3002986, 2012.





BGD
12, 3943–3990, 2015



Meskhidze, N., Chameides, W. L., and Nenes, A.: Dust and pollution: a recipe for enhanced ocean fertilization?, J. Geophys. Res., 110, d03301, doi:10.1029/2004jd005082, 2005.
Moore, J. K. and Doney, S. C.: Iron availability limits the ocean nitrogen inventory stabilizing feedbacks between marine denitrification and nitrogen fixation, Global Biogeochem. Cy., 21, GB2001, doi:10.1029/2006GB002762, 2007.
Myriokefalitakis, S., Vrekoussis, M., Tsigaridis, K., Wittrock, F., Richter, A., Brühl, C., Volkamer, R., Burrows, J. P., and Kanakidou, M.: The influence of natural and anthropogenic secondary sources on the glyoxal global distribution, Atmos. Chem. Phys., 8, 4965–4981, doi:10.5194/acp-8-4965-2008, 2008.
Myriokefalitakis, S., Vignati, E., Tsigaridis, K., Papadimas, C., Sciare, J., Mihalopoulos, N., Facchini, M. C., Rinaldi, M., Dentener, F. J., Ceburnis, D., Hatzianastasiou, N., O'Dowd, C. D., van Weele, M., and Kanakidou, M.: Global modelling of the oceanic source of organic aerosols, Adv. Meteorol., 2010, 939171, doi:10.1155/2010/939171, 2010.
Myriokefalitakis, S., Tsigaridis, K., Mihalopoulos, N., Sciare, J., Nenes, A., Kawamura, K., Segers, A., and Kanakidou, M.: In-cloud oxalate formation in the global troposphere: a 3-D modeling study, Atmos. Chem. Phys., 11, 5761–5782, doi:10.5194/acp-11-5761-2011, 2011.
Nenes, A., Krom, M. D., Mihalopoulos, N., Van Cappellen, P., Shi, Z., Bougiatioti, A., Zarmpas, P., and Herut, B.: Atmospheric acidification of mineral aerosols: a source of bioavailable phosphorus for the oceans, Atmos. Chem. Phys., 11, 6265–6272, doi:10.5194/acp-11-6265-2011, 2011.
Nickovic, S., Vukovic, A., Vujadinovic, M., Djurdjevic, V., and Pejanovic, G.: Technical Note: High-resolution mineralogical database of dust-productive soils for atmospheric dust modeling, Atmos. Chem. Phys., 12, 845–855, doi:10.5194/acp-12-845-2012, 2012.
Nickovic, S., Vukovic, A., and Vujadinovic, M.: Atmospheric processing of iron carried by mineral dust, Atmos. Chem. Phys., 13, 9169–9181, doi:10.5194/acp-13-9169-2013, 2013.
Oakes, M., Ingall, E. D., Lai, B., Shafer, M. M., Hays, M. D., Liu, Z. G., Russell, A. G., and Weber, R. J.: Iron solubility related to particle sulfur content in source emission and ambient fine particles, Environ. Sci. Technol., 46, 6637–6644, 2012.
Olivie, D. J. L., van Velthoven, P. F. J., Beljaars, A. C. M., and Kelder, H. M.: Comparison between archived and off-line diagnosed convective mass fluxes in the chemistry transport model TM3, J. Geophys. Res., 109, D11303, doi:10.1029/2003JD004036, 2004.
Paris, R. and Desboeufs, K. V.: Effect of atmospheric organic complexation on iron-bearing dust solubility, Atmos. Chem. Phys., 13, 4895–4905, doi:10.5194/acp-13-4895-2013, 2013.





BGD
12, 3943–3990, 2015



Paris, R. K., Desboeufs, V., and Journe, E.: Variability of dust iron solubility in atmospheric waters: investigation of the role of oxalate organic complexation, Atmos. Environ., 45, 6510–6517, doi:10.1016/j.atmosenv.2011.08.068, 2011.

Raes, F., Van Dingenen, R., Vignati, E., Wilson, J., Putaud, J.-P., Seinfeld, J. H., and Adams, P.: Formation and cycling of aerosols in the global troposphere, Atmos. Environ., 34, 4215–4240, 2000.

Russell, G. L. and Lerner, J. a.: A New Finite-Differencing Scheme for the Tracer Transport Equation, J. Appl. Meteorol., 20, 1483–1498, doi:10.1175/1520-0450(1981)020<1483:ANFDSF>2.0.CO;2, 1981.

Seinfeld, J. H. and Pandis, S. N.: Atmospheric Chemistry and Physics: From Air Pollution to Climate Change, A Wiley Interscience publication, USA, New York, 1998.

Shao, Y., Wyrwoll, K.-H., Chappell, A., Huang, J., Zhaohui, L., McTainsh, G. H., Mikami, M., Tanaka, T. Y., Wang, X., and Yoon, S.: Dust cycle: an emerging core theme in Earth system science, Aeol. Res., 2, 181–204, doi:10.1016/j.aeolia.2011.02.001, 2011.

Shi, Z., Bonneville, S., Krom, M. D., Carslaw, K. S., Jickells, T. D., Baker, A. R., and Benning, L. G.: Iron dissolution kinetics of mineral dust at low pH during simulated atmospheric processing, Atmos. Chem. Phys., 11, 995–1007, doi:10.5194/acp-11-995-2011, 2011a.

Shi, Z., Krom, M., Bonneville, S., Baker, A. R., Bristow, C., Drake, N., Mann, G., Carslaw, K., McQuaid, J. B., Jickells, T., and Benning, L. G.: Influence of chemical weathering and aging of iron oxides on the potential iron solubility of Saharan dust during simulated atmospheric processing, Global Biogeochem. Cy., 25, GB2010, doi:10.1029/2010GB003837, 2011b.

Shi, Z., Krom, M. D., Jickells, T. D., Bonneville, S., Carslaw, K. S., Mihalopoulos, N., Baker, A. R., and Benning, L. G.: Impacts on iron solubility in the mineral dust by processes in the source region and the atmosphere: a review, Aeol. Res., 5, 21–42, doi:10.1016/j.aeolia.2012.03.001, 2012.

Sholkovitz, E. R., Sedwick, P. N., Church, T. M., Baker, A. R., and Powell, C. F.: Fractional solubility of aerosol iron: synthesis of a global-scale data set, Geochim. Cosmochim. Ac., 89, 173–189, doi:10.1016/j.gca.2012.04.022, 2012.

Sindelarova, K., Granier, C., Bouarar, I., Guenther, A., Tilmes, S., Stavrakou, T., Müller, J.-F., Kuhn, U., Stefani, P., and Knorr, W.: Global data set of biogenic VOC emissions calculated by the MEGAN model over the last 30 years, Atmos. Chem. Phys., 14, 9317–9341, doi:10.5194/acp-14-9317-2014, 2014.





BGD
12, 3943–3990, 2015



Solmon, F., Chuang, P. Y., Meskhidze, N., and Chen, Y.: Acidic processing of mineral dust iron by anthropogenic compounds over the north Pacific Ocean, J. Geophys. Res., 114, D02305, doi:10.1029/2008JD010417, 2009.
Stumm, W. and Morgan, J. J.: Aquatic Chemistry, 3rd edn., J. Wiley-Interscience, New York, 1022 pp., 1996.
Stumm, W. and Sulzberger, B.: The cycling of iron in natural environments: considerations based on laboratory studies of heterogeneous redox processes, Geochim. Cosmochim. Ac., 56, 3233–3257, 1992.
Taylor, S. R. and McLennan, S. M.: The Continental Crust: its Composition and Evolution, Blackwell, Malden, Mass., 312 pp., 1985.
Theodosi, C., Markaki, Z., and Mihalopoulos, N.: Iron speciation, solubility and temporal variability in wet and dry deposition in the Eastern Mediterranean, Mar. Chem., 120, 100–107, doi:10.1016/j.marchem.2008.05.004, 2010.
Tiedke, M.: A comprehensive mass flux scheme for cumulus parameterization in large – scale models, Mon. Weather Rev., 117, 1779–1800, 1989.
Tsigaridis, K. and Kanakidou, M.: Global modelling of secondary organic aerosol in the troposphere: a sensitivity analysis, Atmos. Chem. Phys., 3, 1849–1869, doi:10.5194/acp-3-1849-2003, 2003.
Tsigaridis, K. and Kanakidou, M.: Secondary organic aerosol importance in the future atmosphere, Atmos. Environ., 41, 4682–4692, doi:10.1016/j.atmosenv.2007.03.045, 2007.
Tsigaridis, K., Krol, M., Dentener, F. J., Balkanski, Y., Lathière, J., Metzger, S., Hauglustaine, D. A., and Kanakidou, M.: Change in global aerosol composition since preindustrial times, Atmos. Chem. Phys., 6, 5143–5162, doi:10.5194/acp-6-5143-2006, 2006.
Van Noije, T. P. C., Eskes, H. J., van Weele, M., and van Velthoven, P. F. J.: Implications of the enhanced Brewer-Dobson circulation in European Centre for Medium-Range Weather Forecasts reanalysis ERA-40 for the stratosphere-troposphere exchange of ozone in global chemistry transport models, J. Geophys. Res. D Atmos., 109, 1–13, doi:10.1029/2004JD004586, 2004.
Witt, M., Baker, A. R., and Jickells, T. D.: Atmospheric trace metals over the Atlantic and South Indian Oceans: investigation of metal concentrations and lead isotope ratios in coastal and remote marine aerosols, Atmos. Environ., 40, 5435–5451, doi:10.1016/j.atmosenv.2006.04.041, 2006.





BGD
12, 3943–3990, 2015



Zhu, X. R., Prospero, J. M., Millero, F. J., and Savoie, D. L.: The photochemical reaction in marine aerosol solution and its impact to iron concentration, J. Geophys. Res., 98, 9039–9047, 1993.





BGD
12, 3943–3990, 2015



**Table 1.** Emissions of dust (in $Tg\,yr^{-1}$), dust-minerals (Illite, Kaolinite, Smectite, Hematite and Feldspars; in $Tg\,Fe\,yr^{-1}$), TFe and DFe (in $Tg\,Fe\,yr^{-1}$) used in TM4-ECPL for (a) present (year 2008), (b) past (year 1850) and (c) future (year 2100) simulations.

| Species | Year | Biomass Burning | Anthropogenic | Ships | Soils |
|---|---|---|---|---|---|
| DUST | 2008 | | | | 1090 |
| ILLITE | 2008 | | | | 7.860 |
| KAOLINITE | 2008 | | | | 0.921 |
| SMECTITE | 2008 | | | | 16.100 |
| HEMATITE | 2008 | | | | 5.690 |
| FELDSPAR | 2008 | | | | 2.800 |
| TFe | 1850 | 0.107 | 0.136 | $9.83 \times 10^{-5}$ | 33.400 |
| | 2008 | 1.070 | 0.697 | 0.015 | |
| | 2100 | 1.300 | 0.144 | 0.002 | |
| DFe | 1850 | 0.013 | 0.011 | $7.99 \times 10^{-5}$ | 0.128 |
| | 2008 | 0.127 | 0.059 | 0.012 | |
| | 2100 | 0.154 | 0.012 | 0.001 | |





BGD
12, 3943–3990, 2015



**Table 2.** Constants used for proton-promoted iron dissolution rates and emissions calculations for different types of iron-containing minerals: Water soluble/Dissolved iron (DFe); Fast-released iron ($Fe_F$); Intermediate-released iron ($Fe_I$); Slowly-released iron ($Fe_S$); Refractory iron ($Fe_R$). The parentheses contain the percentage content of Fe type in each mineral.

| Mineral | Fe type | $K_{MIN}$ (mol m$^{-2}$ s$^{-1}$) | $m$ | $A_{MIN}$ (m$^2$ g$^{-1}$) | $K_{eq}$ | $n$ |
|---|---|---|---|---|---|---|
| ILLITE | $Fe_F$ (2.7 %)[a] | $1.17 \times 10^{-09} \exp[9.2 \times 10^3 (1/298 - 1/T)]$[b] | 1[b, c] | 205[b, e] | 41.7 | 2.75 |
| | $Fe_S$ (97.3 %) | $1.30 \times 10^{-11} \exp[6.7 \times 10^3 (1/298 - 1/T)]$[d] | 0.39[d] | 90[d] | | |
| SMECTITE | $Fe_I$ (5 %)[a] | $8.78 \times 10^{-10} \exp[9.2 \times 10^3 (1/298 - 1/T)]$[b] | 1[b, c] | 125[b, e] | 3.31 | 2.85 |
| | $Fe_S$ (95 %) | $8.10 \times 10^{-12} \exp[6.7 \times 10^3 (1/298 - 1/T)]$[d] | 0.3[d] | 300[d] | | |
| HEMATITE | $Fe_R$ (100 %)[b] | $1.80 \times 10^{-11} \exp[9.2 \times 10^3 (1/298 - 1/T)]$[b] | 0.5[e] | 9[b, a] | 0.44 | 2.85 |
| KAOLINITE | DFe(4.3 %)[b] | | | | | |
| | $Fe_R$ (95.7 %) | $1.80 \times 10^{-11} \exp[9.2 \times 10^3 (1/298 - 1/T)]$[f] | 0.1[f] | 20[f] | 0.44[b] | 2.85[b] |
| FELDSPARS | DFe (3 %)[b] | | | | | |
| | $Fe_R$ (97 %) | $1.80 \times 10^{-11} \exp[9.2 \times 10^3 (1/298 - 1/T)]$[f] | 0.5[f] | 1[f] | 0.44[b] | 2.85[b] |

[a] Shi et al. (2011b); [b] Ito and Xu (2014); [c] Lanzl et al. (2012); [d] Ito (2012); [e] Bonneville et al. (2004); [f] Meskhidze et al. (2005).





BGD
12, 3943–3990, 2015



**Table 3.** Constants used for ligand (oxalate)-promoted iron dissolution from Illite and Hematite. Hematite is here used as surrogate for Hematite and Goethite.

| Mineral | Dissolution rates (mol Fe $m^{-2}$ $s^{-1}$) | $A_{min}$ ($m^2$ $g^{-1}$) | Ref. |
|---|---|---|---|
| ILLITE | $3.00 \times 10^{-10}[OXL^{2-}] + 6 \times 10^{-11}$ | 205 | Paris et al. (2011); Johnson and Meskhidze (2013) |
| HEMATITE | $0.36 \cdot (3.00 \times 10^{-12}[OXL^{2-}] - 2 \times 10^{-12})$ $+0.64 \cdot (1.00 \times 10^{-11}[OXL^{2-}] + 7 \times 10^{-13})$ | 9 | Paris et al. (2011); Johnson and Meskhidze (2013) |





BGD
12, 3943–3990, 2015





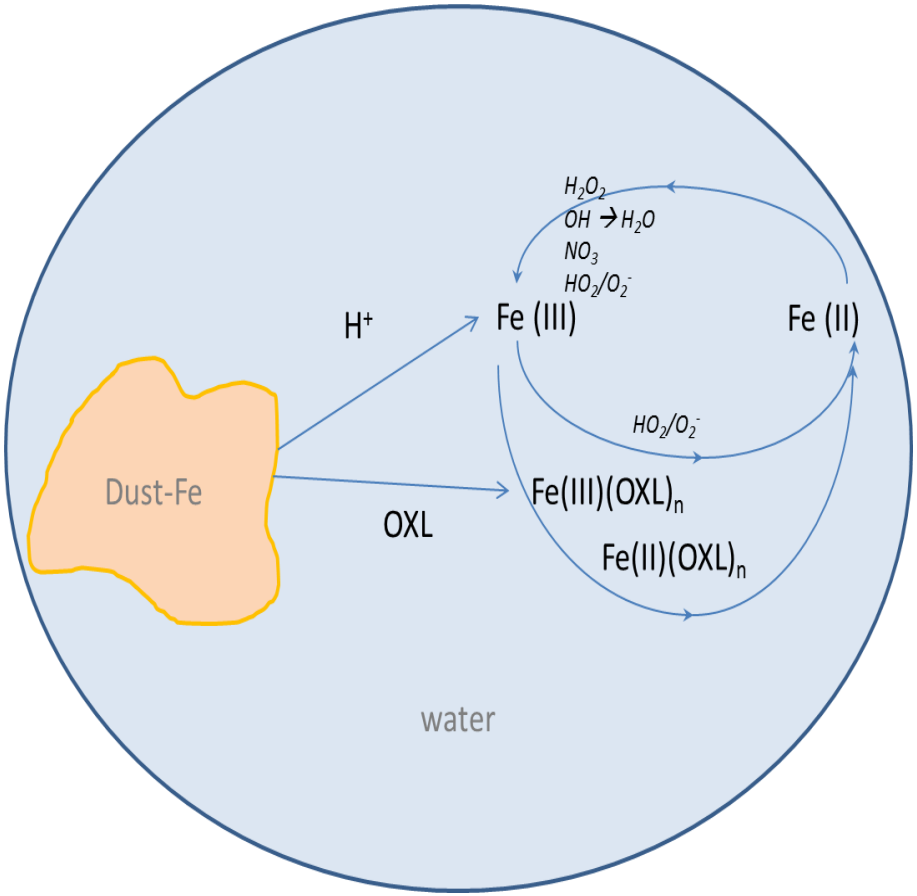


**Figure 1.** Atmospheric processing of dust-Fe taken into account in the model. Details on the chemical reactions are given in Table S2.





BGD
12, 3943–3990, 2015



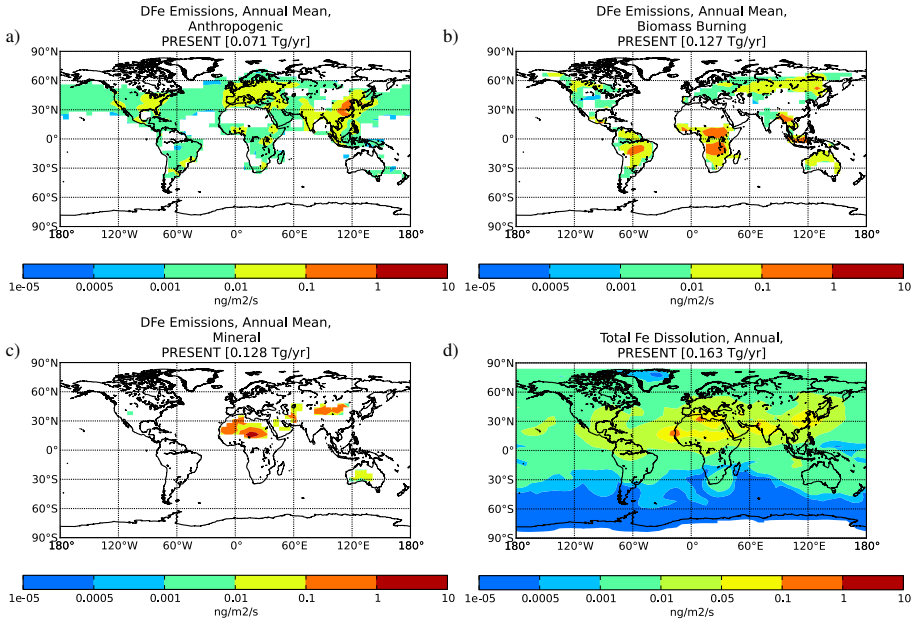


**Figure 2.** Annual averaged distributions (in $\mathrm{ng\,Fe\,m^{-2}\,s^{-1}}$) of **(a)** total anthropogenic DFe primary emissions, **(b)** total biomass burning DFe emissions, **(c)** total DFe mineral emissions and **(d)** total mineral-Fe dissolution flux as calculated by TM4-ECPL for the present atmosphere.





BGD
12, 3943–3990, 2015



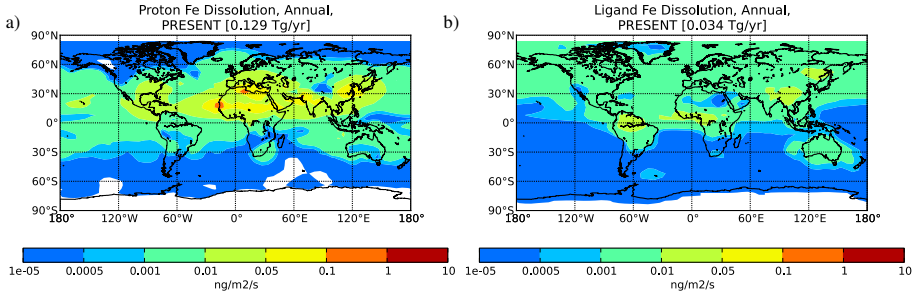


**Figure 3.** Annual averaged **(a)** proton-promoted and **(b)** ligand-promoted mineral-Fe dissolution flux (in ng Fe $m^{-2}$ $s^{-1}$) as calculated by TM4-ECPL for the present atmosphere.





BGD
12, 3943–3990, 2015



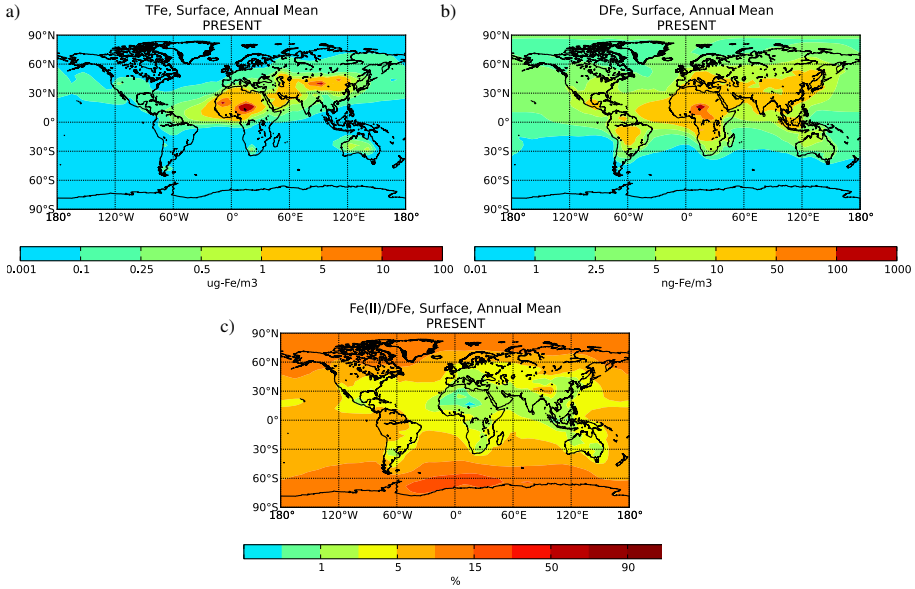


**Figure 4.** Calculated annual mean surface concentrations for the present atmosphere for **(a)** TFe in $\mu g\,Fe\,m^{-3}$; **(b)** DFe in $ng\,Fe\,m^{-3}$ **(c)**; and the %Fe(II) to total DFe fraction (%Fe(II)/DFe).





BGD
12, 3943–3990, 2015



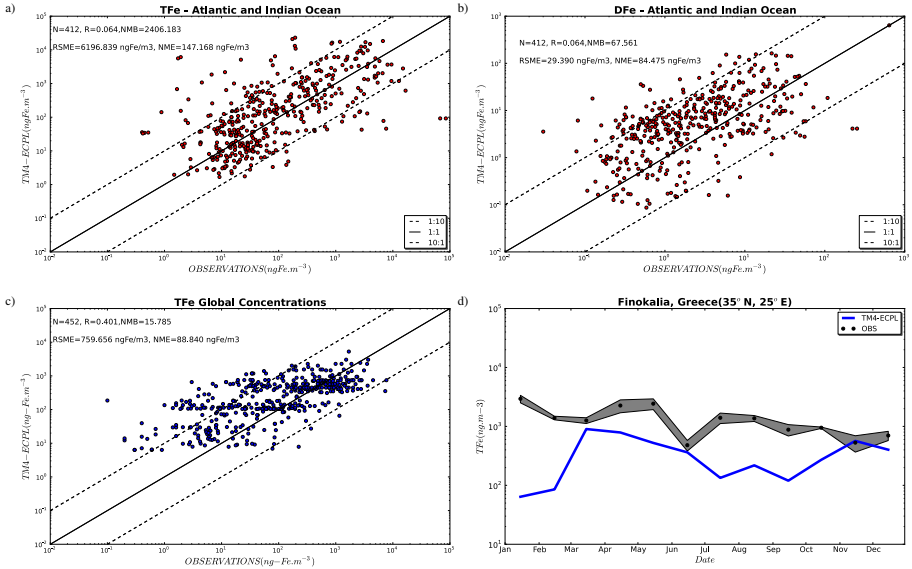


**Figure 5.** Log-scatter plot of model ($y$ axis) comparison with cruises observations over the Atlantic Ocean (Baker et al., 2013) and Indian Ocean (Witt et al., 2006) ($x$ axis) for **(a)** TFe and **(b)** the DFe fractions in ambient aerosols, **(c)** log-Scatter plot of model ($y$ axis) comparison with global observations from Mahowland et al. (2005) and **(d)** timeseries of monthly variation of TFe in ambient aerosols at Finokalia station (Koulouri et al., 2008). In the scatter plots, the continuous black line shows the 1 : 1 correlation, while the dashed lines show the 10 : 1 and 1 : 10 relationships.





BGD
12, 3943–3990, 2015



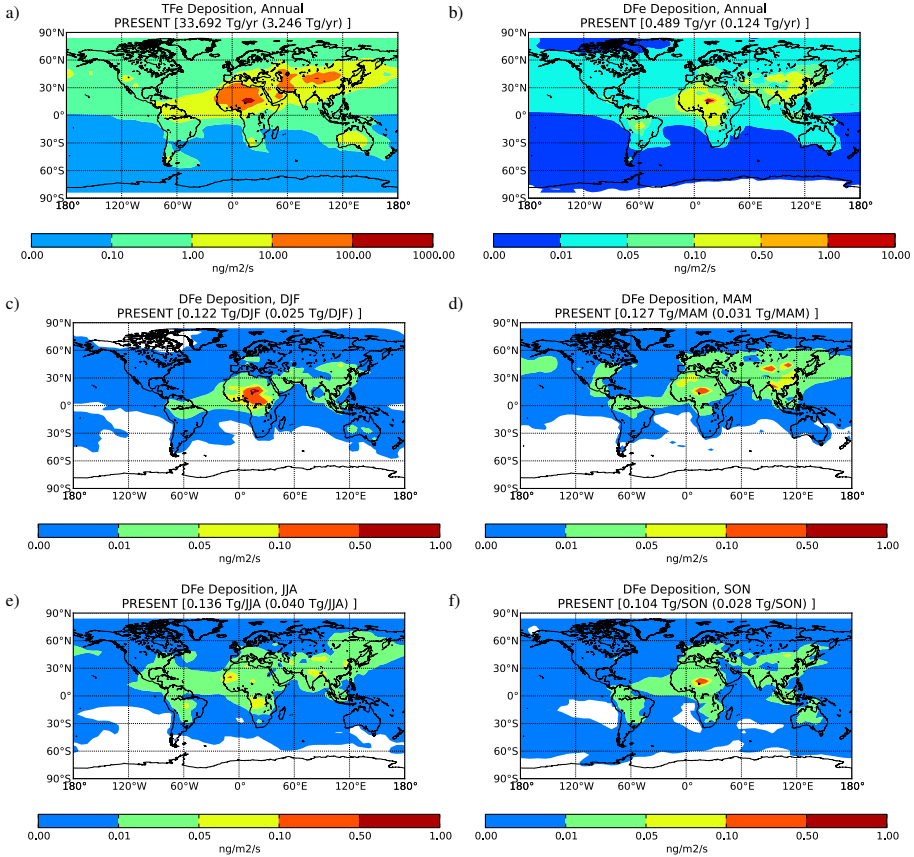


**Figure 6.** Calculated present annual deposition (in ng-Fe $m^{-2}$ $s^{-1}$) for **(a)** TFe, **(b)** DFe, and the seasonal DFe deposition fluxes for **(c)** December, January and February (DJF); **(d)** March, April and May (MAM); **(e)** June, July and August (JJA) and **(f)** September, October and November (SON). In parentheses the amounts of Fe deposition only over oceans are shown.





BGD
12, 3943–3990, 2015

Human-driven changes in dissolved iron deposition to the oceans

S. Myriokefalitakis et al.



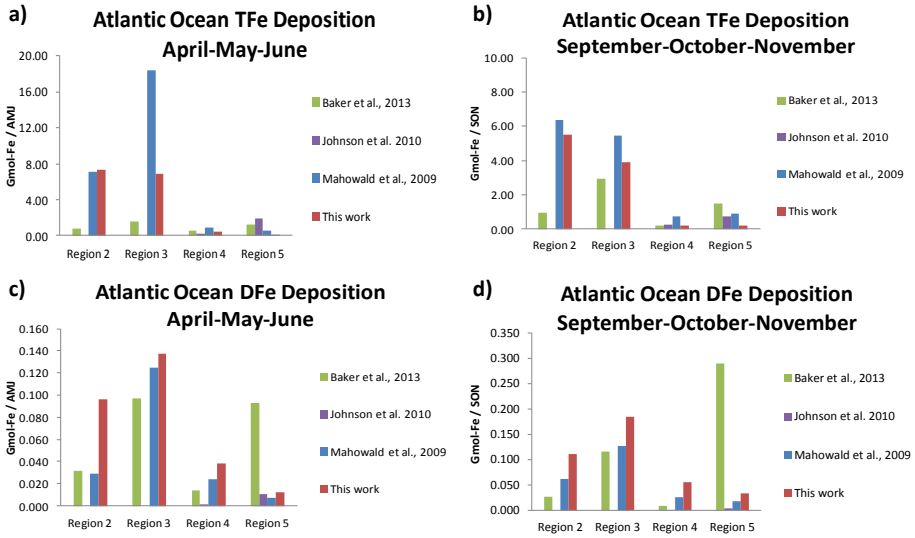


**Figure 7.** Comparison of Total Fe (TFe) and Dissolved Fe (DFe) input estimates to four Atlantic Ocean regions during the April-May-June (AMJ) and September-October-November (SON) periods (in Gmol Fe) as compiled by Baker et al. (2013).





BGD
12, 3943–3990, 2015



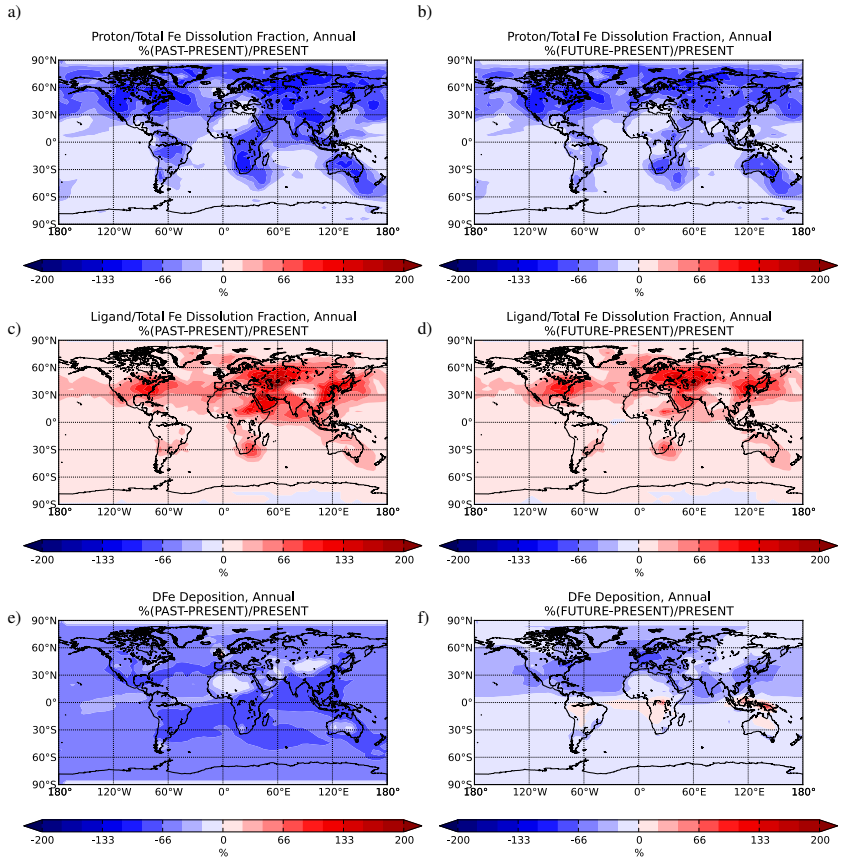


**Figure 8.** The percentage differences of PAST **(a, c)** and FUTURE **(b, d)** simulations from the PRESENT simulation for **(a, b)** Proton-promoted mineral-Fe Dissolution and **(c, d)** Ligand-promoted mineral-Fe Dissolution.





BGD
12, 3943–3990, 2015



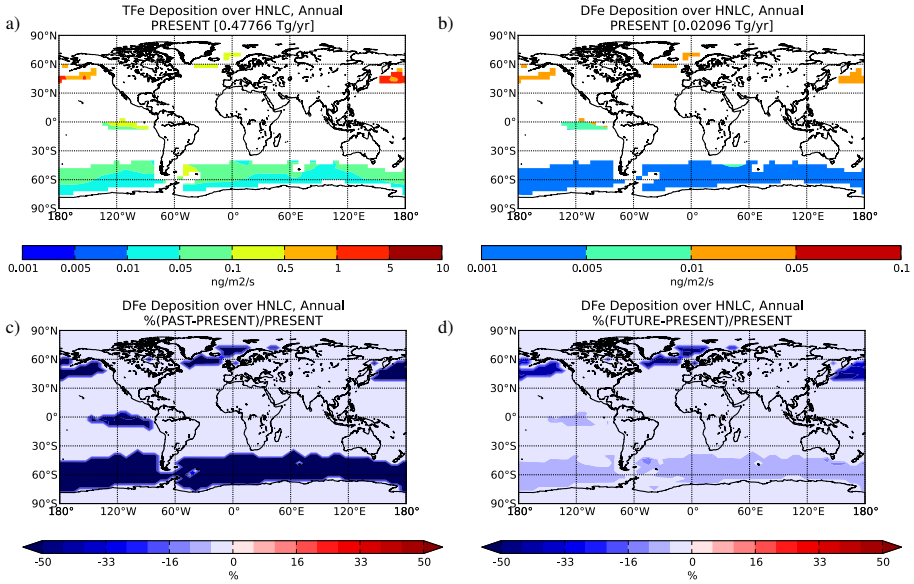


**Figure 9.** The percentage differences of PAST (left panels: **a, c, e**) and FUTURE (right panels: **b, d, f**) simulations from the PRESENT simulation for (**a, b**) Proton-promoted mineral-Fe Dissolution; **(c, d)** Ligand-promoted mineral-Fe Dissolution and **(e,f)** Dissolved Fe (DFe) deposition.





BGD
12, 3943–3990, 2015

Human-driven changes in dissolved iron deposition to the oceans

S. Myriokefalitakis et al.